Properties of the HPSICMECIR Interaction Event of 9–10 September 2011

Al-Shakarchi, Duraid A Mohammed; Morgan, Huw

Published in:
Journal of Geophysical Research: Space Physics

DOI:
10.1002/2017JA024849

Publication date:
2018

Citation for published version (APA):
Al-Shakarchi, D. A. M., & Morgan, H. (2018). Properties of the HPSICMECIR Interaction Event of 9–10 September 2011. Journal of Geophysical Research: Space Physics, 123(4), 2535-2556. https://doi.org/10.1002/2017JA024849

Journal of Geophysical Research: Space Physics

RESEARCH ARTICLE
10.1002/2017JA024849

Key Points:
- An in situ complex interaction between an interplanetary coronal mass ejection (ICME) and corotating interaction region (CIR) is associated with a heliospheric plasma sheet (HPS)
- The CIR is embedded with the ICME and the magnetic field is predominantly open due to an interchange reconnection
- The CIR is compressed by factor of approximately 4 due to the ICME

Correspondence to:
D. A. Al-Shakarchi,
dma3@aber.ac.uk

Citation:
Al-Shakarchi, D. A., & Morgan, H. (2018). Properties of the HPS-ICME-CIR interaction event of 9–10 September 2011. *Journal of Geophysical Research: Space Physics*, *123*, 2535–2556. https://doi.org/10.1002/2017JA024849

Received 3 OCT 2017
Accepted 23 MAR 2018
Accepted article online 30 MAR 2018
Published online 26 APR 2018

Properties of the HPS-ICME-CIR Interaction Event of 9–10 September 2011

Duraid A. Al-Shakarchi[1] **and Huw Morgan**[1]

[1]Institute of Mathematics, Physics and Computer Science, Aberystwyth University, Aberystwyth, UK

Abstract During 9–10 September 2011 the ACE, Wind, and SOHO spacecraft measured the complex interaction between an interplanetary coronal mass ejection (ICME) and a corotating interaction region (CIR) associated with the heliospheric sector boundary. Except for a few short periods, the suprathermal electrons are unidirectional, suggesting that the ICME magnetic field has opened through interchange reconnection. Signatures of interaction are distributed throughout the event suggesting that the structures have become entangled or embedded. Since the ICME speed is relatively low, the strong forward shock must be caused by the ICME-CIR interaction. Other interesting features are the upstream heating flux discontinuity, the very high proton density in the frontal boundary of the heliospheric plasma sheet and the forward shock, the significant speed elevation within the sheath, the distortion of *Bz* in the magnetic cloud, the indistinct location of the stream interface, the unidirectional domination of the suprathermal electrons, and the reverse shock at the CIR rear boundary. There is an unusual delay between the proton density and temperature profiles. Furthermore, large differences in proton speed and forward shock density measured between L1 spacecraft indicate high variation at small spatial scales. A few days earlier, STEREO B recorded the undisturbed CIR, which shows that (i) some general features of the CIR are preserved, (ii) the CIR is compressed by a factor of ~4 by the ICME, and (iii) a magnetic exhausted region at the front of the CIR is a continuous feature and is not formed due to the ICME interaction.

1. Introduction

Coronal mass ejections (CMEs) are eruptions of magnetized plasma from the solar atmosphere, with a broad range of propagation speeds and mass (Gopalswamy & Kundu, 1992; Hudson et al., 1996). Interplanetary coronal mass ejections (ICMEs) are the interplanetary manifestation of CMEs, identified by in situ measurements of the solar wind (Burlaga et al., 1981; Richardson & Cane, 2010; Zurbuchen & Richardson, 2006). Slow, dense solar wind, which manifests itself as streamers or pseudostreamers in the corona, is associated with closed field regions of the Sun (Gosling et al., 1981; Morgan et al., 2013), while the fast, low-density streams arise from open field regions (Krieger et al., 1973). The distribution of slow and fast winds can be complex and changes rapidly during the solar cycle in relation to the magnetic configuration of the photosphere (Morgan, 2011; Morgan & Habbal, 2010). The interaction between streams form compression or rarefaction termed stream interaction regions SIRs (Hundhausen & Gosling, 1976; Parker, 1963; Pizzo, 1978) or corotating interaction regions (CIRs) when an SIR recurs with solar rotation (Gosling & Pizzo, 1999; Jian et al., 2006b).

ICMEs may interact strongly with the ambient solar wind, making precise identification of their boundaries difficult (Gopalswamy, 2006). Two common complex interaction cases are ICME-ICME interaction and ICME-SIR interaction. For example, Burlaga et al. (1987) studied the interaction between a magnetic cloud (MC) and a CIR using three spacecrafts at different longitudes. Lepping et al. (1997) described an event measured approximately 175 R_E upstream of the Earth, consisting of a shock wave observed ahead of an MC whose speed exceeded the ambient solar wind speed. Furthermore, the MC was followed and overtaken by a CIR that compressed the rear of the MC and a two-stream interface (SI) observed an hour later. Significant to this case was the sudden rise in the magnetic field magnitude from 21 nT to 30 nT within the MC and an abnormal twin-peaked density in the solar wind following the MC. The sudden increase of the MC magnetic field could have been the result of CIR-induced compression at the rear boundary of the MC. The CIR interaction with the MC may have produced an instability, which formed a complex boundary. Alternatively, it might have been part of another solar event or the high stream interaction with the current sheet. This ambiguity highlights the difficulty of interpreting complex interacting streams and ICMEs.

Wei et al. (2003) studied many cases of interaction between MCs and the ambient solar wind, concluding that these interactions complicate the identification of the MC boundaries. Another well-studied case of ICME-CIR interaction occurred during the passage of an MC following a CIR during January 1997 (Burlaga et al., 1998). Its most remarkable feature was a very high density and $^4He^{++}/H^+$ ratio in the rear of the MC originating from the prominence material core of the CME. The further development of ICME-HSS interaction studies was made possible by the Sun Earth Connection Coronal and Heliospheric Investigation (Howard et al., 2002) instruments on board the Solar Terrestrial Relations Observatory (STEREO; Kaiser, 2005), in particular the heliospheric imagers (HIs). Rouillard et al. (2009) used HIs to identify the geometry of CIRs and their interaction with ICMEs at 1 AU based on HI-1B and HI-2B time-differenced images of the 19 July 2007 event. Farrugia et al. (2011) studied a complex MC-CIR interaction near the heliospheric current sheet on 19–20 November 2007. Multiple spacecraft measurements enabled a reconstruction of the flux rope structure and clear signatures of forward and reverse shocks near Earth.

Often associated with CIRs are sector boundaries (SBs), or the heliospheric current sheet (HCS), between large-scale regions of inward and outward directed magnetic fields (Svalgaard & Wilcox, 1975; Wilcox & Ness, 1965). SBs are associated with increased ion flux, plasma density, and a decreased solar wind speed (Blanco et al., 2006; Crooker et al., 2004; Khabarova & Zastenker, 2011). In the context of ICME-SIR interaction regions, the identification of a single sector boundary becomes more difficult or impossible. Furthermore, there is often considerable mismatch between sector boundaries identified by magnetic field reversals and those identified by electron polarity reversals (Crooker et al., 2002; Kahler & Lin, 1994, 1995). For example, Crooker et al. (1996) found 14 reversals of the magnetic field during 2 days of measurements and proposed a multiple flux tube structure resulting in pockets of "false" polarities and a folded heliospheric current sheet.

CME-coronal hole interaction can result in interchange reconnection between the closed magnetic loops of CMEs and a neighboring open field (see, e.g., Crooker et al., 2002, 2004; Fisk, 2005; Harra et al., 2007; Wang & Sheeley Jr, 2003). Interchange reconnection leads to localized magnetic field reversals near sector boundaries, particularly in the presence of ICMEs. In the case of closed neighboring field lines, a partial disconnection will be the dominant mechanism. Gosling et al. (1995) used interchange reconnection to explain the unidirectional heating flux (strahl) beams associated with opened field lines in ICMEs resulting from partial disconnection. By analyzing 48 MCs, Shodhan et al. (2000) found sizeable signatures of open magnetic field at 1 AU and suggested a process of continual interchange reconnection, which continued until the ICMEs became completely open.

Winslow et al. (2016) conclude that caution should be exercised regarding geomagnetic storm forecasting that depends upon ICME magnetic field observations close to the Sun, especially when there is an interaction with corotating structures, because this interaction could change the morphology of the magnetic field measurements. They studied HPS/HCS-ICME interaction using MESSENGER (Andrews et al., 2007) and STEREO A observations and found a turbulent region within the STEREO A MC flux rope observations; however, no change in MESSENGER data was observed. They attributed this turbulence to the ICME- HPS/HCS interaction during the ICME propagation through interplanetary space.

This study investigates the properties and characteristics of three large-scale interacting structures (a CIR, associated with a HPS, and an ICME) and seeks to measure the extent to which this interaction affects their magnetic field and plasma properties. In section 2, we present the remote sensing and in situ instruments; in section 3, we examine the coronal observations of the 6 September CME observation, and its L1 in situ interplanetary magnetic field and plasma observations on 9 September, also examine the HPS, HCS, SBC, and the CIR in situ measurements. In addition, the section included a comparison with a CIR recorded in 4 September 2011 by STEREO B in the absence of an ICME. Conclusions are given in section 4.

2. Instruments

Remote sensing observations used in this study are made by the C2 instrument of the Large Angle Spectroscopic Coronagraph (LASCO; Brueckner et al., 1995) on board the Solar and Heliospheric Observatory (SOHO; Domingo et al., 1995), and the COR 2 coronagraph of STEREO A. Extreme Ultraviolet (EUV) images of the low corona are from the Atmospheric Imaging Assembly (AIA; Lemen et al., 2011) instrument aboard the Solar Dynamics Observatory (SDO; Pesnell, 2015). Photospheric magnetic map observations are made by the Helioseismic and Magnetic Imager (HMI/SDO; Scherrer et al., 2011). These remote

Table 1
The in Situ Magnetic Field and Solar Wind Plasma Instruments of ACE, Wind, STB, and SOHO

Spacecraft	Magnetic field instrument	Solar wind plasma instrument
ACE	Magnetic field experiment, MAG (Smith et al., 1998)	Solar Wind Electron Proton Alpha Monitor, SWEPAM (McComas et al., 1998)
Wind	Magnetic field investigation, MFI (Lepping et al., 1995)	Solar Wind Experiment, SWE (Ogilvie et al., 1995)
STEREO B	In situ Measurements of Particles and CME Transients, IMPACT (Luhmann et al., 2008)	Plasma and Suprathermal Ion Composition, PLASTIC (Sauvaud et al., 2008)
SOHO	-	Charge, Element, and Isotope Analysis System/Mass Time-of-Light, CELIAS/MTOF (Ipavich et al., 1998)

observations are used to provide context and to interpret the in situ measurements made by spacecraft near Earth.

The in situ data are from the Advanced Composition Explorer (ACE; Stone et al., 1998) and Wind spacecrafts near L1. The in situ instruments are listed in Table 1. The proton density is missing or contains data gaps in the ACE 64-s cadence data. The ACE 5-min browse is available but not suitable for the scientific studies, so it has used the SOHO/CELIAS 5 min.

There are large gaps also in the corresponding Wind 1-min magnetic field and plasma measurements. Wind observations, when available, are used for comparison with ACE.

The suprathermal electron pitch angle distributions measured by SWEPAM-E/ACE are provided at 10 energy channels ranging from 73 eV to 1.37 KeV. Here we use the 272-eV channel because data at that energy are typically representative of the suprathermal population, although lower energies can still be part of the thermal core distribution, depending on conditions. Higher energies are more prone to contamination by energetic particles or other effects, and the count rates are typically lower. The low counts can also mean that the high energies are more sensitive to errors arising from combining data from detectors with very different gains. This study also used in situ measurements, which are mentioned in Table 1.

Since the ACE magnetometer and SOHO proton measurements are available throughout the event, they are shown together for the purpose of comparison in many figures. From the relatively close locations of the three L1 spacecraft as shown in Figure 1, similar measurements would be expected. However, as will be shown, significant differences are seen during some periods. Large differences over small spatial scales have also been reported for Helios measurements for two spacecraft separated by only 1° latitude in the same coronal hole (Schwenn, 1990). Based on STEREO and ACE measurements, Rouillard et al. (2009) found different CIR speed profiles over small latitudinal ranges.

3. Results

3.1. Eruption and Low-Coronal Propagation

Figure 2 shows the solar disk as observed in EUV during 6 September 2011. A large active region (NOAA AR11283), the source of the ICME under study, is situated at N14 W18, with a complex beta-gamma-delta configuration. Also of relevance to this study is the equatorial coronal hole to the east of the meridian (CH475).

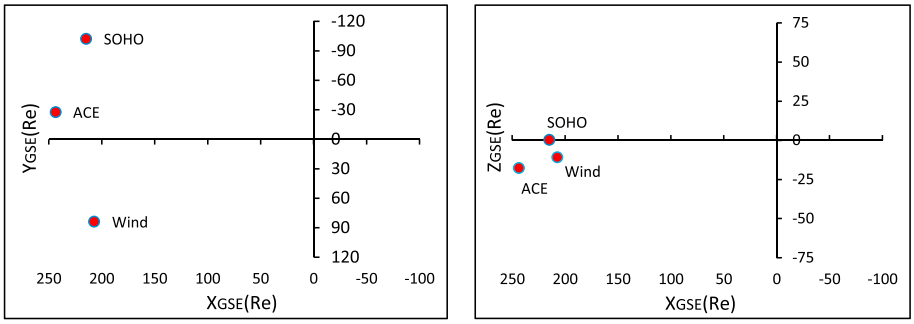

Figure 1. The L1 spacecraft positions ACE, Wind, and SOHO on 9 September 2011 (1 Re = 6,371.2 km).

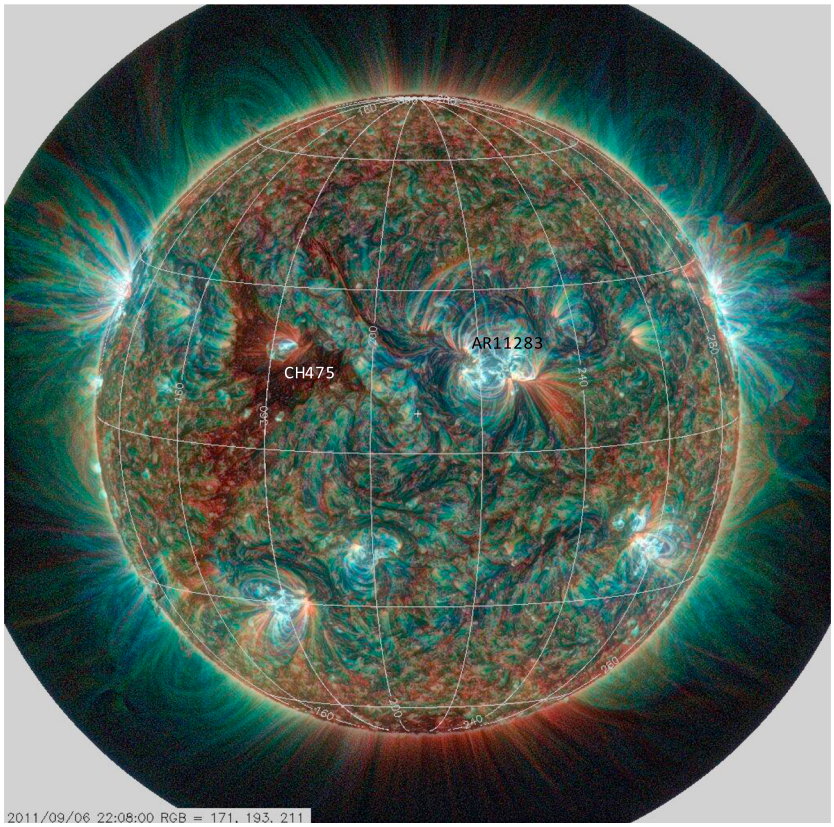

Figure 2. Composite EUV image of the solar disk and low corona made using AIA/SDO observations during 6 September 2011 12:00. The three-color red-green-blue image channels are composed of observations made in three AIA channels: 171 Å, 193 Å, and 211 Å, respectively, corresponding to their most dominant emission lines of Fe IX, Fe XII, and Fe XIV with formation temperatures ~0.7, 1.2, and 2.0 MK. The images have been processed using Multiscale Gaussian Normalization (Morgan & Druckmüller, 2014).

The coronal hole extends from latitude −25° to 30° and is 15° wide in longitude. The coronal hole is a persistent feature for several rotations and is the source of a CIR. During 6 September, there is two halo CME that erupted at 02:24 UT from the location N14 W07 and 23:05 UT from the location N14 W18 (the first one mentioned in SOHO/LASCO catalog as poor event. Also, on 7 September, there are two partial halo CMEs that erupted at 18:48 UT from the location N23 E54 and 23:05 UT from the location N14 W28. It has tested the estimated transit times of these CMEs based on the onset times and speed and the space speed. The 6 September 23:05 UT CME is optimized to matching with the 9 September ICME. Its estimated transit time is about 61 hr (with space speed about 680 km/s). This value is close to Wu et al. (2016) who have tested these four CME candidate sources of the ICME 9 September 2011 forward shock that emitted during 6 and 7 September 2011, erupted from N17 W07, N14 W18, N23 E54, and N14 W28.They concluded that the 6 September (N14 W18) is the most likely driver of the 9 September ICME forward shock.

As shown in the AIA/SDO sequence of Figure 3, there is a sigmoid magnetic structure (indicative of a twisted flux tube/toroid instability) embedded within the heart of the west footpoint of the active region. The sigmoid is clearly seen at 22:03. Immediately following there is a very rapid (impulsive) eruption, and a postflare arcade appears by 22:51 UT. Associated with the eruption is a massive X2.1 flare on 6 September, 22:20 UT, accompanied by Types II and IV radio bursts. The preeruption configuration and initial stages of the eruption have been simulated in detail using a nonlinear force-free model by Jiang et al. (2013). They suggest that reconnection at the null-point cuts overlying tethers and probably triggers the torus instability of the flux rope, which results in the eruption.

At around 23:00 UT, the CME of interest from AR11283 appears as a fast halo CME in the LASCO C2 field of view, shown in the top row of Figure 4. This is a halo CME skewed toward the northwest corona. In the LASCO C2 image, part of the halo CME shares the field of view with the previous three-part CME in the

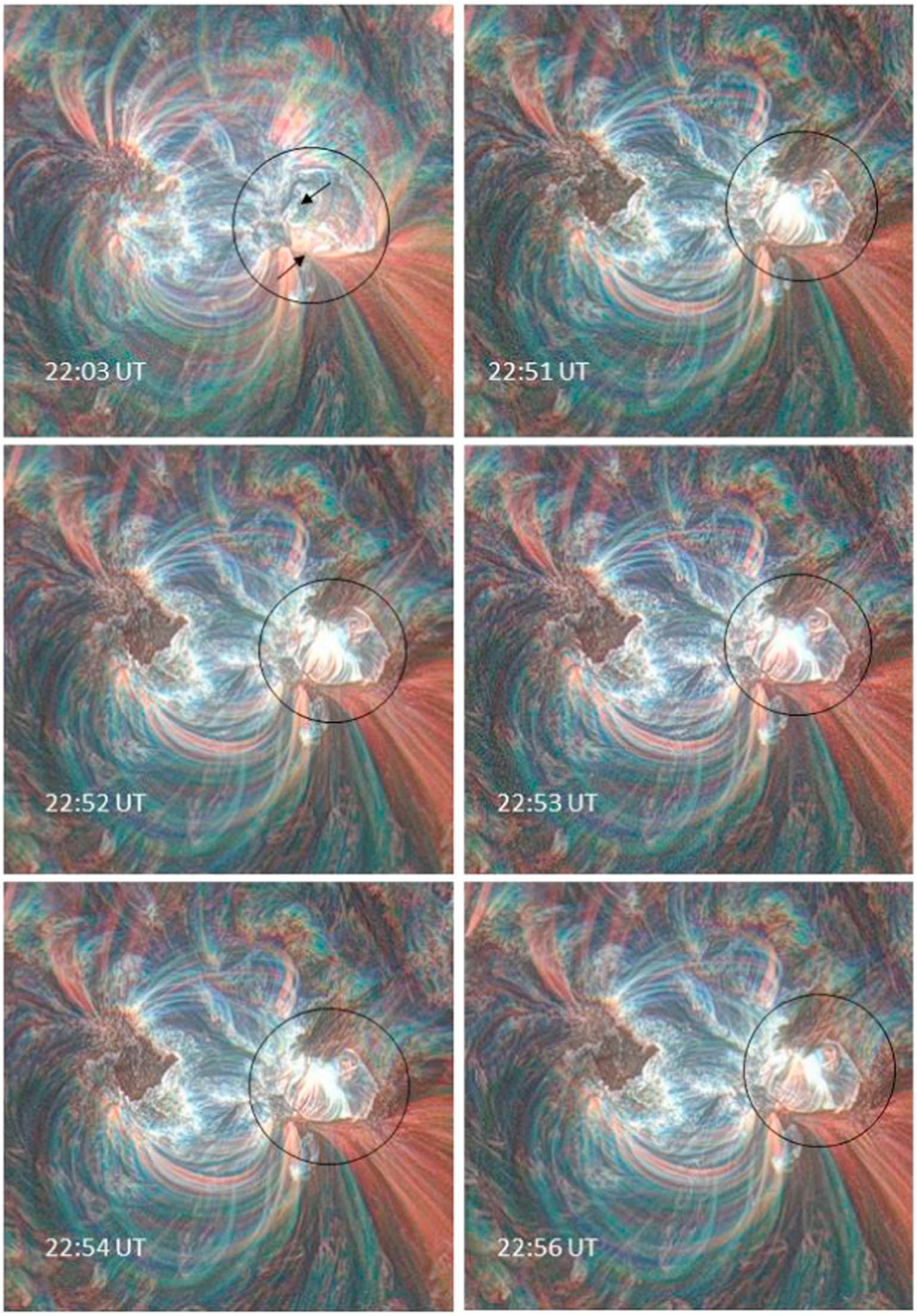

Figure 3. The 6 September 2011 AR11283 flux rope. The upper left panel desplays the S sigmoid at 22:03 UT, whereas the other panels show the magnetic flux rope sequence for a few minutes. These images have been processed using Multiscale Gaussian Normalization. The two arrows on the upper left panel determine the two ends of the S sigmoid, and the the black circles on all panels display the flux rope progress position during the panels times.

northwest, making it difficult to interpret its structure. The bottom row of Figure 3 shows the same CME as viewed by STEREO COR2 A.

From this viewpoint, the bulk of the CME of interest is seen just northward of the equator. The other three-part CME is at apparent high latitude, with only a small overlap between the two. The large CME from

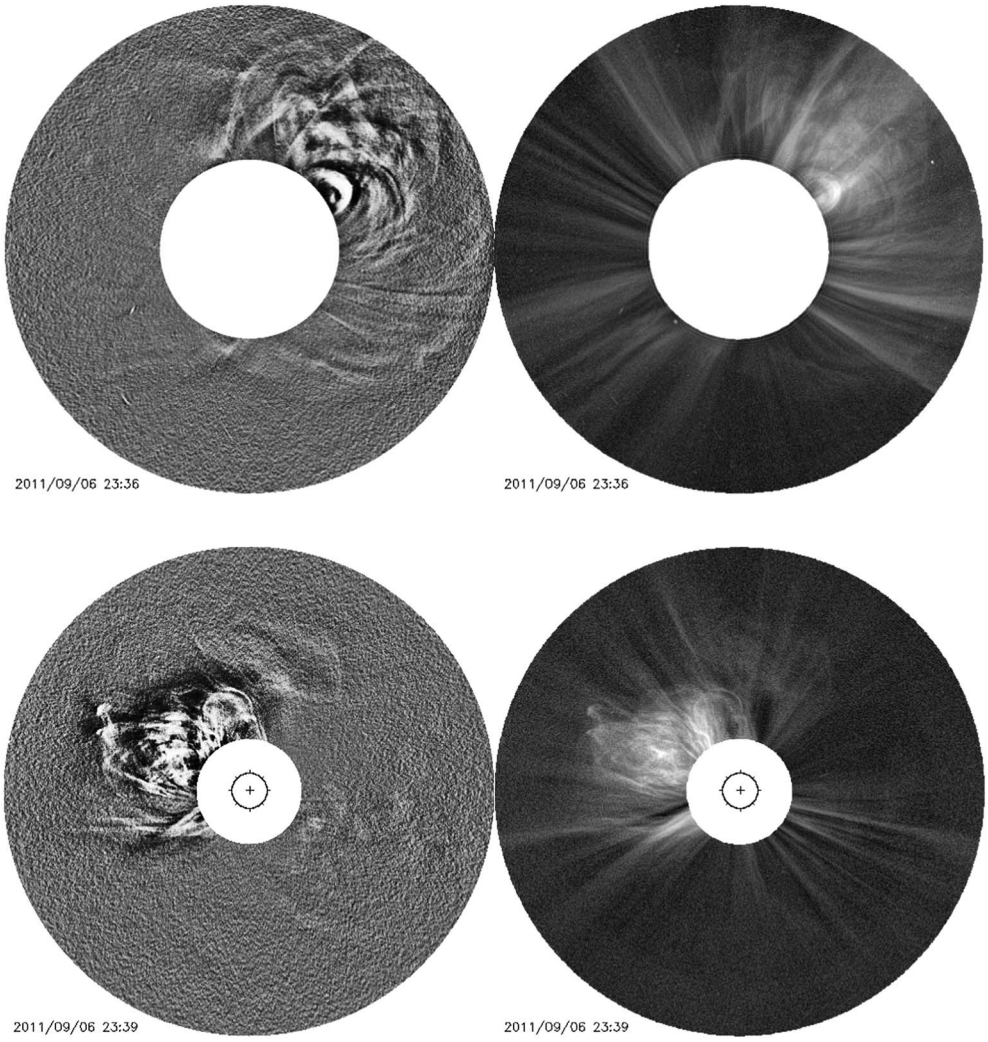

Figure 4. Top row shows a LASCO C2 image of 6 September 2011 23:36, showing a halo CME skewed towards the northwest and a previous three-part CME in the northwest. Bottom row shows a STEREO COR2 A image of 6 September 2011 23:39. The CME of interest is distributed from around −30 to +60 from the equator. The previous three-part CME is at high latitude, although there is some overlap between the two CMEs. The left images have been processed using a Dynamic Separation Technique to remove quiescent radial structure (Morgan & Habbal, 2010), and the right images have been processed using the Normalizing Radial Graded Filter of Morgan et al. (2006).

AR11283 has an extremely complicated structure, seemingly composed of a main frontal system of distinct loops. These propagate outward at high speed. Behind, or within, these loops are myriad dense clouds of material that may be interpreted as the CME core. This is not a compact core sitting tidily near the CME center—it is distributed as several spread-out blobs across a wide portion of the CME. Hours after the main front of the CME has passed from the COR2A field of view, sizeable, fast, and dense material continues to propagate outward. The last sizeable blob passes out of the field of view at around 05:00 UT on 7 September 2011. The central latitude of the CME is around 20° north, and although the bulk of the CME lies north of the equator, there is considerable material propagating along the equator. The southern extremity of the CME is approximately 30° south.

3.2. ICME in Situ Measurements

ACE in situ plasma and magnetic field measurements are displayed in Figure 5 for 9 September 00:00 UT to 11 September 12:00 UT, spanning the occurrence of the ICME arising from the 6 September 2011 eruption (the proton density data are from SOHO/CELIAS). The ICME is interacting with the SIR arising from the equatorial

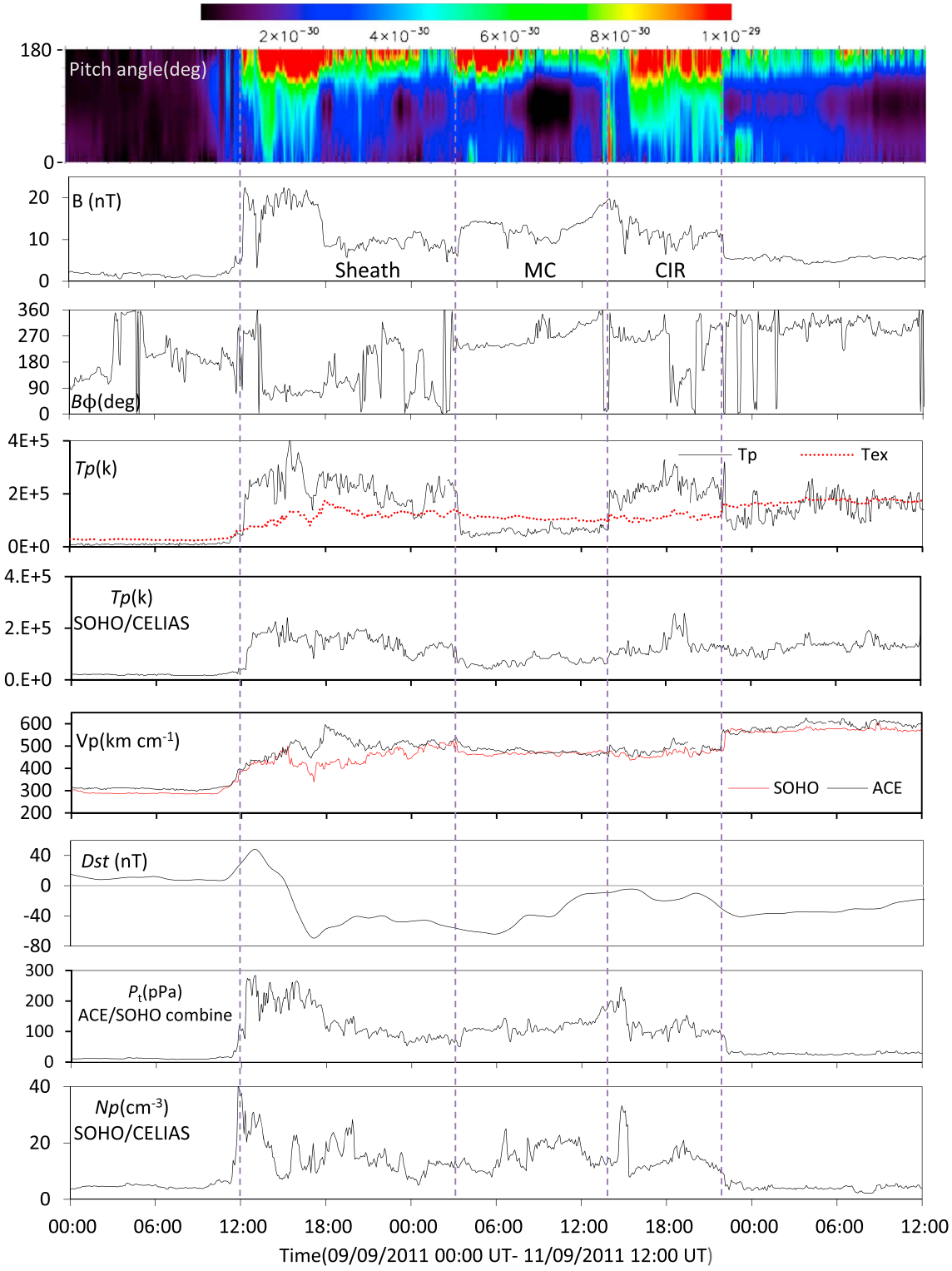

Figure 5. The event magnetic field and plasma parameters. From the upper panel: the ACE color-coded electrons pitch angle distributions $f(v)$ (cm^{-6}/s^3) at 272-eV energy (color coding for $f(v)$ is logarithmic and ranges from 5×10^{-31} s^3/cm^{-6} [dark blue] to 2×10^{-29} s^3/cm^{-6} [dark red]). Magnetic field strength B (nT), $B\phi$ (deg), proton temperature T_p (°K), SOHO proton temperature T_p (K), ACE (black) and SOHO (red) proton speed V_p (km/s), Dst index (nT), ACE/SOHO combine total pressure P_t (pPa), and proton density N_p (cm^{-3}) from SOHO.

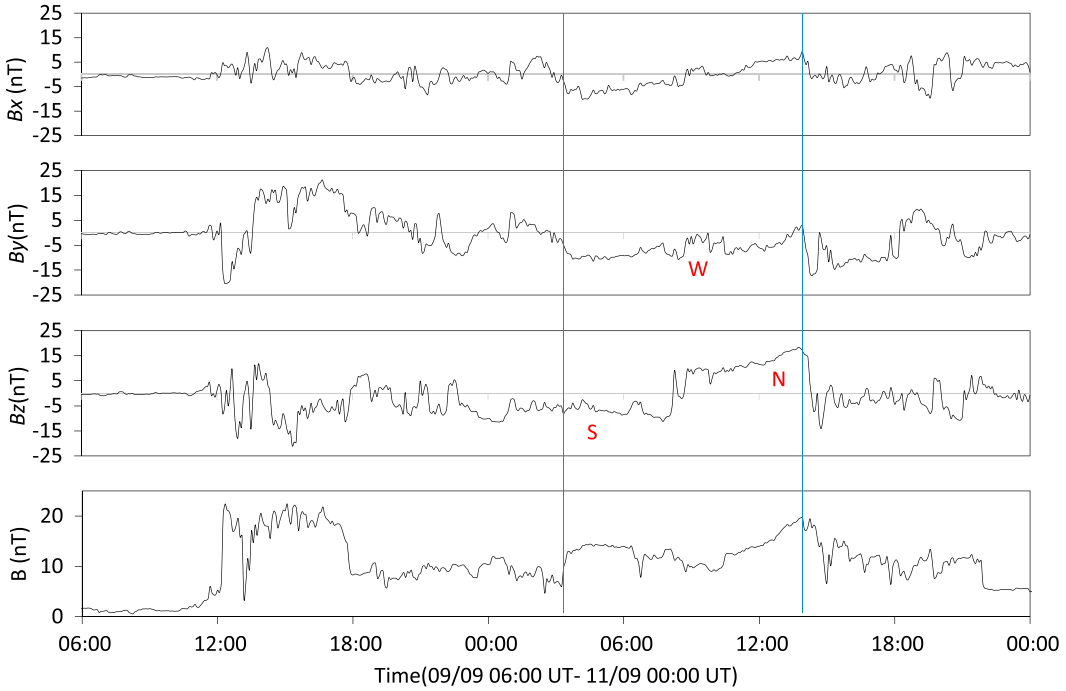

Figure 6. The interplanetary magnetic field vectors (*Bx*, *By*, and *Bz*) and their directions through the MC. Blue vertical lines are the MC boundaries. The symbols W, S, and N refer to the flux rope directions: west, south, and north respectively.

coronal hole 475 seen in Figure 2. This interaction region is clear, given the values of the solar wind flow speeds immediately following the disruption of the ICME, which reaches a maximum of >600 km/s.

During 9 September, both the ACE and Wind spacecrafts recorded multiple inversions of the azimuthal magnetic field and a frontal large increase in density (SOHO and Wind), plasma beta (Wind) (see Wind magnetic and plasma morphology for 9 September in Figure 10), and solar wind speed elevation, consistent with an interplanetary forward shock (first vertical dashed line). The increase in the magnetic field magnitude during the shock and the sheath region exceeded 20 nT at times. This shock seems extremely strong, inconsistent with ideal MHD. Later in this paper we attribute the strength of the shock to the interaction between the ICME and the CIR (sections 3.6 and 3.8). The ICME was geoeffective (*Dst* ~ −69 nT). The ICME is driving a forward shock as the cloud front boundary speed relative to the upstream solar wind exceeded the magnetosonic speed (50–70 km/s). The shock passes over ACE on 9 September 2011 12:14 UT and is followed by a sheath. The solar wind proton temperature jumps from 4.63×10^4 to 1.98×10^5 K and is accompanied by increases in the following: magnetic field strength from ~5 to 20 nT, proton density to values of about 40 cm^{-3} (from SOHO), and proton flow speed. The sheath duration is very long (over 15 hr), suggesting that ACE is traversing the ICME flank. This is largely consistent with the configuration of the CME as viewed by coronagraphs in the low corona.

A distinct region of the ICME follows the sheath, bounded by the second and third vertical lines at 10 September 2011, 03:30 UT and 14:00 UT, and is characterized by an abrupt reduction of proton temperature to values lower than the ambient solar wind (Richardson & Cane, 2010), a magnetic field strength increase from 6.2 to 14.4 nT and an azimuthal magnetic field $B\phi$ rotation. The *Tp/Tex* ratio (Richardson & Cane, 1995) was used to identify the magnetic cloud MC boundaries. The magnetic field component during this period, shown in more detail in Figure 6, reveals a coherent rotation in the *Bx* and *By* components and a less clear rotation in *Bz*. These characteristics suggest that ACE is traversing the main flux rope (magnetic cloud) region of the ICME. The magnetic field vectors rotate for 10.5 hr through an angle >30°. The sudden variation of *Bz* in the midpoint of the MC is maybe due to the ICME-SIR interaction, which can distort the flux rope while maintaining the general helical field topology (Zhang et al., 2013).

Within the magnetic cloud, the *By* component has a unipolar negative polarity as the *Bx* and *Bz* components rotate from negative to positive (south to north). From this, the MC has a south-west-north (SWN) signature

and has a right-hand (RH) helicity as viewed by an observer looking toward the Sun (Bothmer & Rust, 1997; Mulligan et al., 1998), and the *Bz* bipolar signature exhibits an elliptically aligned magnetic flux rope (Mulligan et al., 1998). The short duration of the flux rope, preceded by a long sheath duration, may support the scenario of the spacecraft passing through the ICME flank (qualitatively matching track 4 of Gopalswamy (2006) where the spacecraft traverse through the shock, sheath, and finally the MC from the flank). The ACE/SOHO combined total perpendicular pressure profile (P_t) can give an indication of the distance of the spacecraft path from the ICME center. P_t increases at the leading edge of the ICME (Figure 5) followed by a long plateau and then another increase at the rear part of the ICME. This P_t morphology matches the Group 2 morphology of Jian et al. (2006a) and Russell et al. (2005) and confirms that the spacecraft traverses the ICME flank.

3.3. CIR Measurements

The transequatorial coronal hole CH475 (Figure 2) persists for several rotations and is the source of the CIR that follows the ICME, readily identified by an overall increase in the solar wind velocity, an enhancement of proton density, temperature, a peak of total pressure, and compression of the magnetic field magnitude (Jian et al., 2006b; Neugebauer et al., 2004; Siscoe & Intriligator, 1993). The MC rear speed is slower than the following fast wind, and there is an interaction region at the rear boundary of the MC, including what seems like a slow shock (Figure 5, third vertical line), seen at 10 September 2011, 13:59 UT and characterized by an increase in proton temperature, an abrupt increase in density, and a drop in the magnetic field magnitude. The CIR ends with a distinct fast reverse shock at 21:54, identified by a clear increase in proton speed and a decrease in the magnetic field magnitude and temperature. The formation of the reverse shock and the apparent front slow shock within 1 AU is due to the existence of the ICME (see, e.g., Gosling et al., 1976; Smith & Wolfe, 1976) (more details in section 3.7). The high-speed stream (HSS) follows the CIR reverse shock. The proton speed increases abruptly from 480 to 559 km/s and exceeds 615 km/s after about 5 hr, and the HSS of CH475 continues for a few days.

The presence of the CIR and HSS may have affected the ICME bulk speed morphology. The decrease of the ICME speed (from almost 600 km/s) within the sheath to ~450 km/s at the trailing edge of the MC indicates an overall deceleration of the ICME from the low coronal speed and an expansion of the structure. The size of the sheath is estimated as ~0.18 AU, and that of the MC as ~0.12 AU are less than the typical sizes at 1 AU, despite the continual expansion. This expansion suggests that besides the possibility of the spacecraft's trajectory passing through the flank, the ICME may have witnessed a deflection due to the neighboring coronal hole (CH475 high stream) and the SIR overtaking the rarefied region of the MC (e.g., (Gopalswamy et al., 2009).

3.4. Geomagnetic Response

During the ICME-CIR arrival at Earth, the magnetosphere was under the influence of both structures. Panel 7 of Figure 5 shows the *Dst* index, which increases with the arrival of the ICME in response to the shock compression (*B* magnitude peaked to 20–22 nT). On 9 September 2011 15:00, the main phase (which represents the ring current injection) started with a substantial decrease of *Dst* values to <-69 nT—a moderate storm. The main phase occurs in response to the southward interplanetary magnetic field, when *Bz* dipped to 21 nT south, and followed by a recovery phase where the *Dst* increased gradually until 10 September 2011 16:00, including a substorm. In response to the CIR, the *Dst* varied and dropped again to -41 nT on 10 September 2011 23:00 UT, followed by the CIR recovery phase.

3.5. Heating Flux Distribution and Interchange Reconnection

Panel 1 of Figure 5 shows the suprathermal electron pitch angle distribution at 272-eV energy in the solar wind frame. In general, the suprathermal electrons are unidirectional with a 180° pitch angle, except at a few times at the CIR boundaries. The unidirectional strahl displays a temporal variation with a sporadic broad intense strahl (between 40° and 50°) at the front region of the sheath, MC, and during the CIR duration. The strahl became narrower during the rarefied region of the MC and after the CIR reverse shock. We notice that 90° electron depletions are observed on all three days. The appearance of the 180° unidirectional pitch angle during the ICME-CIR passage suggests that the ICME magnetic field lines are predominantly open, which is probably due to interchange reconnection between ICME and the neighboring coronal hole.

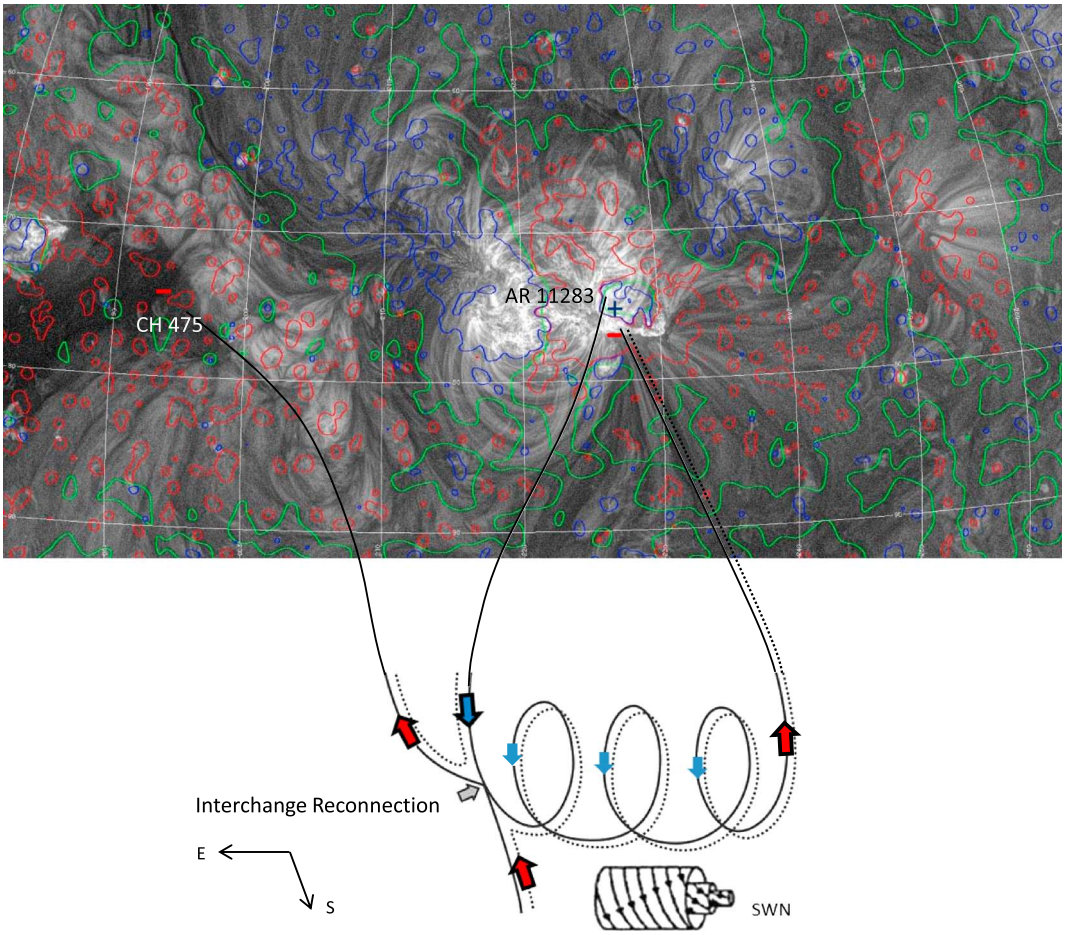

Figure 7. The photospheric magnetic field map of 6 September 2011 and a schematic of the magnetic flux rope structure. The EUV image is by AIA/SDO, and the photospheric field measurement is gained through Gaussian smoothing of HMI/SDO. It also illustrates interchange reconnection (IR) between the 6 September CME from AR11283 and coronal hole CH475. Coronal hole inward field lines diverge toward the flux rope leg outward field line, and an IR has occurred. Red arrows refer to the inward field line, blue arrows refer to the outward field lines, and grey arrows refer to the sites of IR (modified from Harra et al., 2007).

Figure 7 highlights the solar photospheric magnetic field map and a schematic of the MC flux rope structure and its footpoints. The flux rope has an SWN signature rotation with a right-hand (RH) helicity. The map displays the negative (inward) rooted polarity of the MC left leg and the positive (outward) leg polarity of the right.

During its interval, the MC local magnetic field longitude $B\phi$ was steady (hovering between inward and orthogonal with an inward domination of ~315° (in accordance with the Parker spiral distribution of the interplanetary magnetic field). Since the suprathermal electron distribution remained unidirectional at 180° (opposite to the magnetic field direction), and the strahl always travels away from the Sun, it can determine the overall magnetic direction as an inward and the left MC inward leg as the immersed side of the flux rope in the photosphere. Figure 7 suggests an interchange reconnection scenario: In conjunction with the growth and expansion of the closed flux loop, the negative and inward CH475 open field lines might swerved or diffused toward the photospheric area where the closed magnetic field lines domination and intercepted the propagation of the ICME neighbor outward leg field lines, making the MC completely open during the passage of the spacecraft at 1 AU. This view is supported by the suprathermal electrons streaming distribution within the MC, which stayed antiparallel to the magnetic field.

The sporadic, short periods of counterstreaming electrons are likely due to (1) energized electrons leaking from the enhanced flux CIR shock boundaries into the upstream solar wind, producing a "field-aligned"

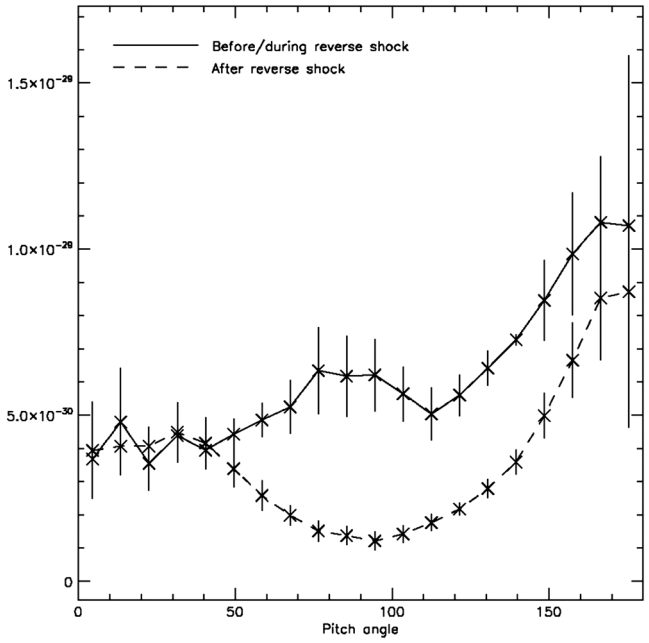

Figure 8. The pitch angle distributions of the suprathermal electrons before/during (solid line) and after (dashed line) the CIR reverse shock. The depletion around 90° is clear after the shock arrival. Each profile is the median of distributions measured over a period of around 9 hr before and after the shock. The error bars show the standard deviation of values during this 9-hr period.

beam of electrons, which take the outward direction from both CIR shocks (see, e.g., Gosling et al., 1993; Steinberg et al., 2005), and (2) depletions around a 90° pitch angle as a result of magnetic focusing and mirroring (Gosling et al., 2001), particularly after the CIR reverse shock e.g. (Skoug et al., 2006). Before the CIR reverse shock there is a unidirectional antiparallel stream (at a 180° pitch angle) (Figure 5 panel 1). Immediately after the CIR reverse shock, the suprathermal electrons pitch angle distribution displays a 90° depletion (Figure 8), associated with a strahl enhancement at a 180° pitch angle. This is likely due to energizing at the CIR reverse shock and a leak in the sunward direction into the upstream solar wind (Steinberg et al., 2005).

It is likely that interchange reconnection led to multiple field reversals within both the HCS and the sheath (Figure 5, panel 3) while the suprathermal electrons remained at a 180° pitch angle (panel 1). Since the strahl usually travels away from the Sun, the overall magnetic field direction of the event remained inward, even with the presence of the local magnetic reversals. This result implies that the pitch angle distributions of the suprathermal electrons are independent of any local magnetic field line torsion, not just in the HCS area but also in the ICME sheath. In addition, the duration of reversals in the sheath was longer than those in the HCS, despite the high sheath compression by both the HCS at the front and the MC, CIR, and HSS at the rear.

3.6. HPS/HCS-ICME Interaction Region

On 8 September 2011, the suprathermal electron pitch angle distribution was parallel to the magnetic field. During 9 September 02:00 UT to 09:00 UT (Figure 9 panel 1), there are a series of heat flux dropouts (HFDs), a signature of magnetic reconnection, or electron pitch scattering. From approximately (09:00 UT to 11:30 UT), the upstream suprathermal electrons showed a distribution peaking at 90° followed by a discontinuity of electron heat flux, likely a shock, coinciding with a clear rising of plasma density and beta (Figure 9 panel 3 and Figure 10 panels 3 and 6). This is the appearance of the initial boundary of the heliospheric plasma sheet (the first blue vertical line in Figure 9).

The heat flux discontinuity seems to be indicative of the arrival of a high-speed solar wind stream (HSS). After about 30 min (12:14 UT), ACE showed spikes in magnetic field, proton temperature, and a 180° heat flux enhancement referring to an ICME forward shock (the brown dashed vertical line). During this time (at 11:44 UT), the 180° pitch angle distribution of the suprathermal electrons first appeared (the red dotted vertical line in Figures 9 and 10), indicating a sector boundary crossing (SBC) and associated with $B\phi$ flipping from outward to inward, which means that the heliospheric current sheet (HCS) had the same SBC position (SBC-HCS matching).

For further clarification, we designate the green-shaded region as region A in Figure 9. This is the HPS, which has two boundaries (two vertical blue lines) identified by three main criteria: an enhancement in proton density, plasma beta enhancement, and the inversion of the interplanetary magnetic field sector (see, e.g., Crooker et al., 2004; Liu et al., 2014; Simunac et al., 2012; Suess et al., 2009; Winterhalter et al., 1994). For the purposes of comparison and to compensate for missing ACE data, Wind data are shown in Figure 10. At the HPS boundaries, two spikes in plasma beta can be seen: the first peaking at approximately $\beta = 11$ in Wind and the second at $\beta = 28$ in Wind (ACE data are missing). These are associated with a high reduction of the magnetic field magnitude and discontinuities of the heating flux.

The sector boundary lies at the point at which the suprathermal pitch angle distributions change (Liu et al., 2014). In ideal conditions, the SBCs appear to synchronize with the HCS, but in many previous instances this has not been the case (see, e.g., Crooker et al., 1996; Kahler et al., 1996). This mismatch has been attributed to many processes associated with magnetic reconnection such as heat flux dropout (McComas et al., 1989) or interchange reconnection (Crooker et al., 2002). The SBC start time was at the same time for all SWEPAM

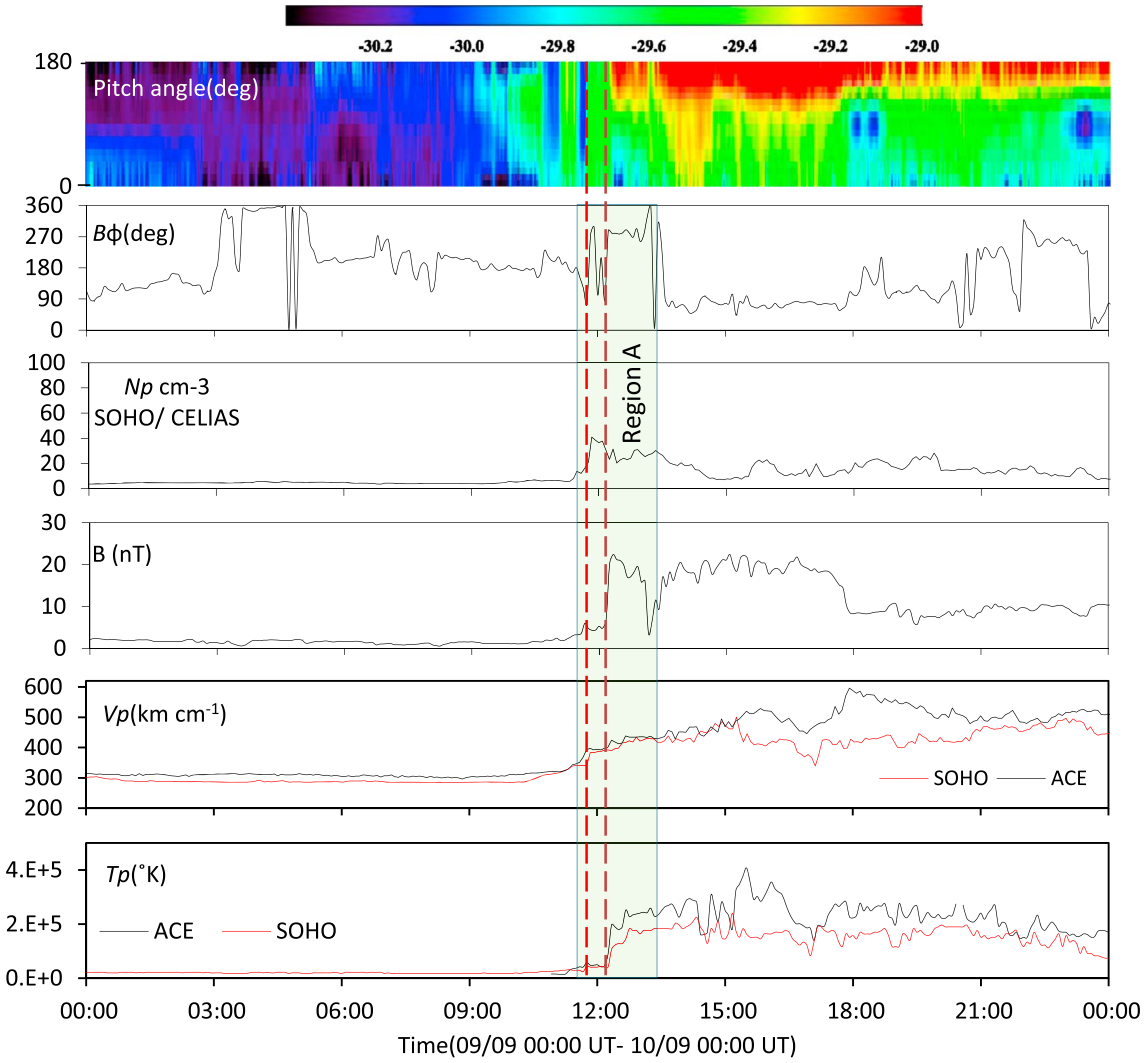

Figure 9. This figure highlights the Ace and SOHO region A where the HPS, HCS, SBC, and the ICME forward shock occurs (the SOHO proton density profile is to cover the ACE missing data). From top to bottom, the panels show heat flux distribution, $B\varphi$, N_p, B, ACE (black) and SOHO (red) proton speed V_p (km/s), and ACE (black) and SOHO (red) proton temperature T_p (K). The two blue vertical lines refer to the HPS boundaries, the dotted red vertical line refers to the SBC-HCS region, and the brown dashed vertical line refers to the ICME forward shock. Note that the heat flux distribution (top panel) shows the electron flux on a log scale to visualize variations of low signals.

energy channels. The HCS location bordered the first HPS's boundary (the HPS did not straddle the HCS), supporting our finding that interchange reconnection is a dominant process. Guerrero et al. (2012) reference an SBC location at about 13:19 UT without referring to the HCS or HPS. We rule out the possibility of the SBC being located at this position because the first appearance of the 180° pitch angle of the suprathermal electrons precedes it by more than 1.5 hr. On the other hand, it is possible that the HCS was located at this position (SBC-HCS mismatching) because of the azimuthal magnetic field reversal, the plasma beta spike of the second boundary of the heliospheric plasma sheet, and the dynamic and total pressure balance, which were clear in Wind observations (Figure 10).

The important features of the plasma and magnetic field measurements made by all three spacecrafts within this interaction region are summarized as follows:

1. The region begins with a small increase of proton speed (from 321 to 394 km/s), magnetic field magnitude (from 2.5 to 7 nT), thermal velocity (from 18.3 to 29.3), and total pressure (from 0.02 to 0.05 nPa) associated with a high increase of proton density, reaching 40/cm^3 at SOHO and exceeding 90/cm^3 at Wind. Despite

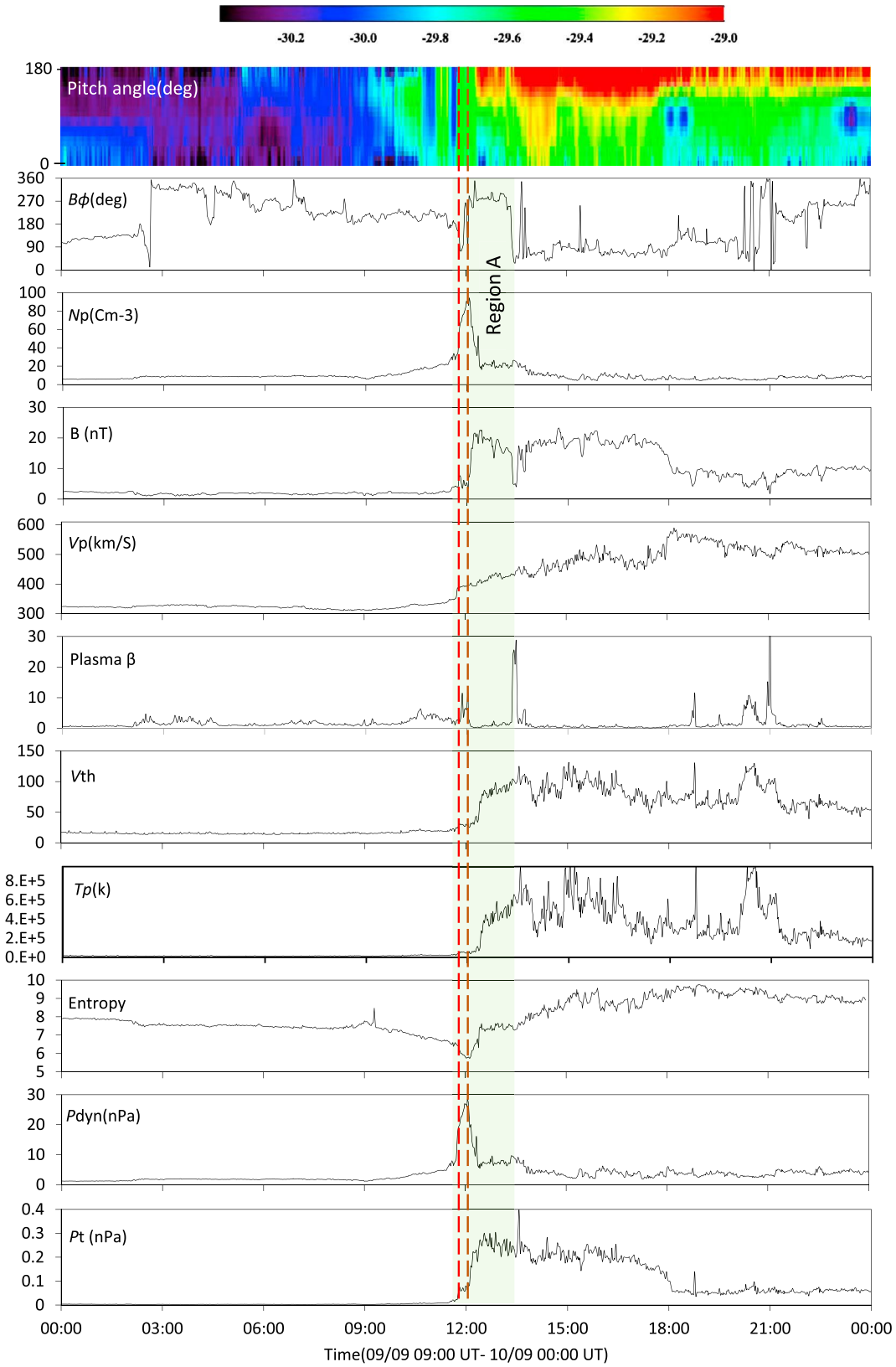

Figure 10. Properties of region A as measured by Wind. From top to bottom: heat flux distribution (measured by ACE), $B\varphi$, N_p, B, V_p, plasma beta, Vth, T_p (K), entropy, dynamc pressure (nPa), and P_t (nPa). The ACE suprathermal electron distribution is included (first panel) for comparison. The dotted red line refers to the SBC-HCS region, and the dotted brown vertical line refers to the ICME forward shock.

resampling the higher-time-resolution proton data of Wind to match the 5-min sampling of SOHO, this considerable difference in density remains. The SOHO density decreases at the brown dashed line, where the Wind density peaks and decreases later, roughly coincident with the temperature change. There is a delay of about 13 min between the temperature increase at ACE/SOHO and the temperature increase at Wind. However, the increase in the magnetic field magnitude occurs at the same time at both ACE and Wind. The differences between ACE/SOHO and Wind are likely due to the small separation between spacecraft (and thus high local variations in the event's properties) and/or to variations in the IMF (Weimer et al., 2002, 2003; Weimer & King, 2008).

We attribute the high proton density at the first HPS boundary to interchange reconnection between the ICME and the neighboring coronal hole open field, which releases a stream of discontinuous plasma parcels into the HPS-ICME interaction region, at the front of the ICME shock, similar to Song et al. (2009), Rouillard et al. (2010), and Wang et al. (2000). The second significant increase of magnetic strength, proton temperature (at ACE and SOHO) and total pressure occurs around 30 min after the initial increase, and this is the forward shock. Because of its low speed, it is not possible for the ICME to drive this forward shock. The most likely source of the shock is the ICME-CIR interaction. The impact of the interaction is the suprathermal discontinuity at the front boundary of the HPS, the first small increase in proton speed, magnetic field magnitude, thermal velocity, and total pressure, and the noticeable increase of speed within the ICME sheath (see section 3.8).

2. The ICME forward shock speed is low due to its position within the HPS, which decelerates and delays the shock inside the HPS (see, e.g., Hu & Jia, 2001; Mitsakou & Moussas, 2014; Smith, Odstrcil, et al., 1998). This low speed is perhaps due to energy dissipation during the passage of the forward shock through the HPS (Watanabe, 1989), which reflected on the narrow electron heating flux at the shock position.
3. The density decrease after the shock is due to either a bulk movement of material to the front boundary of the HPS through interchange reconnection or the dissipation that we mentioned in point 2 above. In addition, the high-level density at the HPS front boundary, when compared to the shock density, exaggerates the decrease. The presence of the magnetic strength, total pressure, and proton temperature increase supports the existence of this shock at this position.
4. At the onset of the HPS, Wind experience a decline in entropy (Figure 10), followed by a sharp rise during the ICME forward shock passage, before stabilizing between the shock and the second HPS boundary, due to stable density and temperature. This entropy behavior, where the increase occurs within the HPS, is rather different from the cases documented by Simunac et al. (2012), in which an increase is reported at the second HPS boundary. We attribute this difference to the existence of the ICME forward shock within the HPS.
5. The total pressure increased at the onset of the first HPS boundary until the ICME shock. This is unprecedented in previous studies of HPS (Crooker et al., 2004; Winterhalter et al., 1994), which consistently observe total pressure stability within the HPS. This contrast is due to HPS penetration to the ICME front and subsequent influence of the forward shock. This varying total pressure stabilizes after the shock passage because the change in magnetic pressure is balanced by a corresponding change in plasma thermal pressure (Winterhalter et al., 1994).
6. Both the forward shock and the HPS have their imprint on each other. The existence of the forward shock within the HPS changes some of its behaviors and vice versa. Their physical parameters are different than when both are individual.

3.7. CIR Compression Due To the ICME

The yellow shaded region in Figure 11 is supposed to be a transformation area between the ICME rear and the 10 September CIR lasting for about 80 min and distinguished by a steep drop in magnetic field magnitude and a significant rise in plasma density and temperature. The first impression refers to a magnetic reconnection exhaust region (Gosling et al., 2005), where magnetic field energy is converted into a plasma flow energy (Gosling et al., 2006; Xu et al., 2011).

There is a limited bidirectional pitch angle distribution of suprathermal electrons around the front boundary. We attribute this to the high heating at this first boundary although the general state of this event was unidirectional; however, the second boundary maintained a unidirectional field. In addition, the strahl witnessed a reduction in 180° heating flux distribution during this region; by contrast it was higher before the first boundary (during the MC duration) and more intense with broader beam high energies after the second

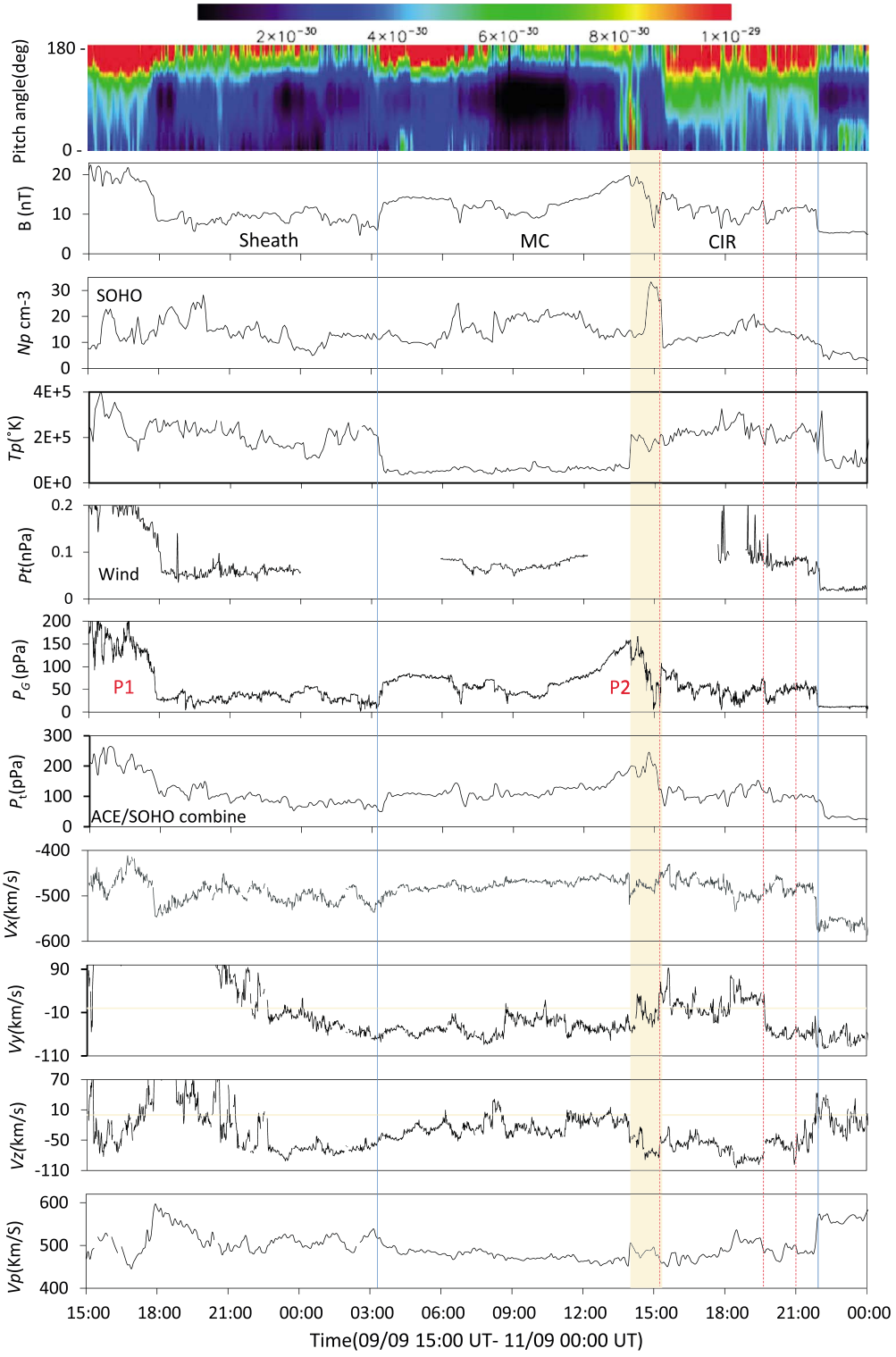

Figure 11. The ICME-CIR interaction region (yellow area). From the top panel: ACE suprathermal electrons pitch angle distributions (deg); magnetic field magnitude B (nT); proton density N_p (cm^{-3}; from SOHO); proton temperature T_p (K); total pressure P_t (pPa; from Wind); magnetic pressure P_G (pPa); ACE/SOHO combined data of total pressure P_t (pPa); and solar wind velocity three components in GSE coordination (km/s): Vx, Vy, Vz, and proton speed Vp (km/s). Purple vertical line refers to the MC onset, the green vertical line is the CIR reverse shock, and the three dotted red vertical lines are the nominated SIs. P1 and P2 in the sixth panel are the two magnetic pressure peaks at the front and rear boundary of the ICME.

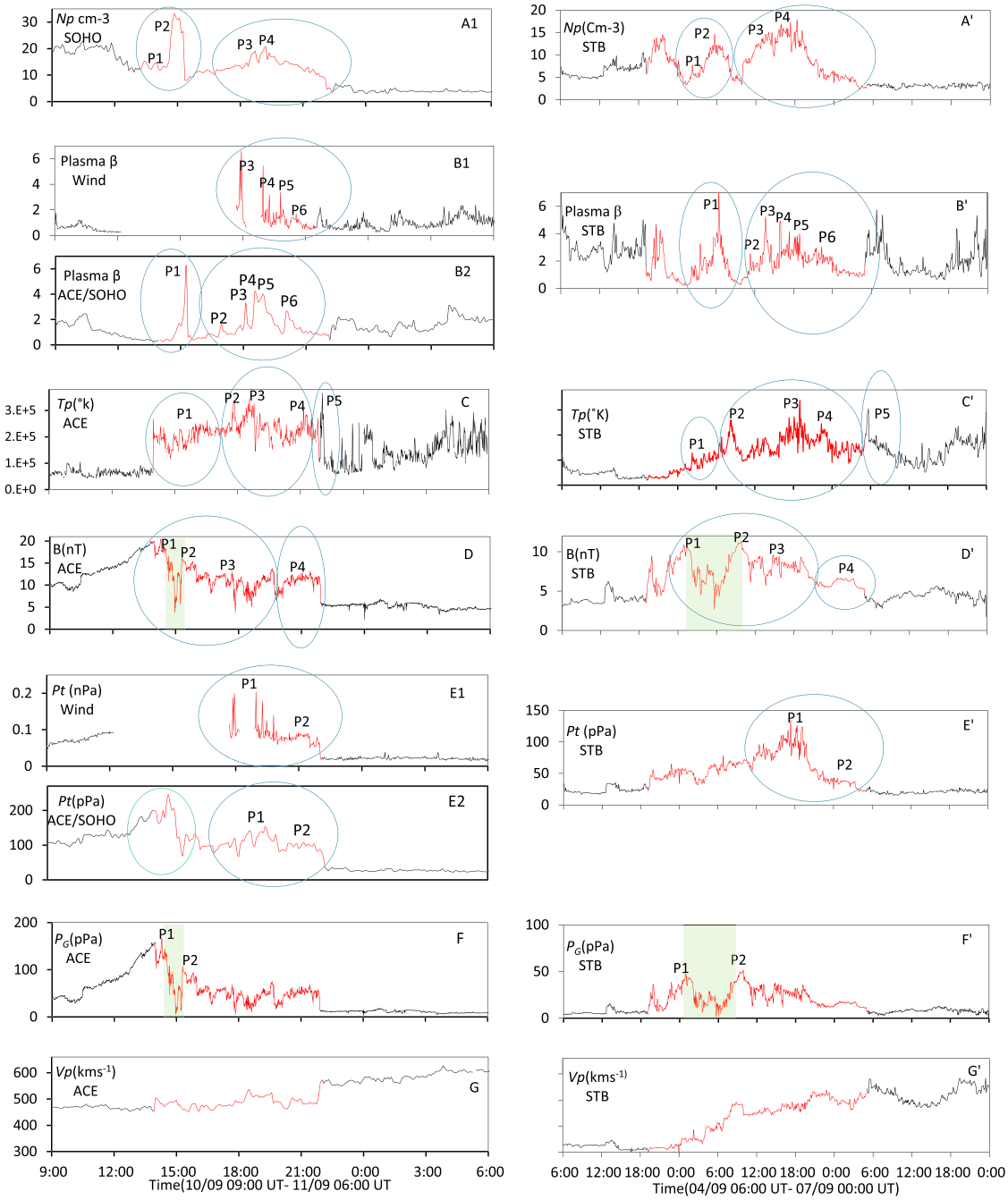

Figure 12. Left panels: CIR L1 spacecraft data of N_p (cm^{-3}) from SOHO, plasma beta from Wind, plasma beta from ACE/SOHO combine,T_p (°K) from ACE, B (nT) from ACE, total pressure P_t (nPa) from Wind, total pressure P_t (pPa) from ACE/SOHO combine, magnetic pressure P_G (pPa), and proton speed (km/s) from ACE for the period (10 September 09:00 UT to 11 September 06:00 UT). Right panels: CIR STB data with the same magnetic field and solar wind parameters for the period (4 September 06:00 UT to 7 September 00:00 UT).

boundary. The different characteristic of this region compared with the two-bounded large interplanetary structures has to do with it being a transition region with its own individual properties. The appearance of the shock-like structure may be attributed to two causes: (1) the high ICME-CIR compression and (2) the interplanetary shock, which was recorded by STB on 4 September at 12:38 UT with Mach no. 1.34.

To evaluate the interpretation of the CIR and the transformation region observations, a comparison was made with the same CIR measured in the absence of an ICME by STEREO B on 4 September 2011 19:00 UT.

STEREO B had an ~95° separation angle east to the Earth and measured a total CIR duration of approximately 34 hr. A comparison of the behaviors of the CIR by STEREO B and then by L1 spacecraft reveals many similarities in their properties, despite the interaction described above. The left and right sides of Figure 12 show the available measurements of the CIR by the L1 and STEREO B spacecraft, respectively. We identify similar features between the two sets of measurements by the blue oval shapes, with the "P" labels showing peaks or plateaus. The most significant patterns are as follows:

1. In panel A1, we label four distinct peaks in SOHO proton density by P1–P4 and their counterparts in STEREO B in panel A′ and note that the STEREO B CIR duration was approximately 34 hr in comparison to an SOHO CIR duration of approximately 8 hr (all L1 spacecrafts have the same duration). A comparison of panels B1(Wind plasma beta) and B′ similarly shows four pairs of matching peaks of plasma beta. Because of Wind missing data, P1 and P2 do not appear in B1 panel. For just comparison, it has used the ACE/SOHO combine data (panel B2). It displays a noticeable P1 that is missing on panel B1. C/C′ shows the comparison of proton temperature.
2. Similarly, panels D and D′ reveal four pairs of magnetic field matches between ACE and CIR STB. The two green-shaded areas in D and D′ reveal a magnetic reduction region within the STB CIR and indicate that the magnetic exhaust region in the ICME-CIR compression region is already present before the interaction. From this, it may be concluded that the role of ICME-CIR interaction is merely to compress and reduce the duration of this exhaust region. This runs counter to our previous conclusion that the ICME-CIR interaction is responsible for the creation of the exhausted region. Furthermore, this result suggests that care must be taken in the interpretation of many other similar cases. Accurate interpretation of many complex in situ interaction events is difficult without a comparison of events in the absence of interaction.
3. Panel E1 shows the total pressure morphology from Wind (albeit with a few hour data gap). There is a match between E1 and E′ at both P1 and P2. For verification, the ACE/SOHO combined data profile E2 displays the same P1 and P2 and a significant large peak of the total pressure at the CIR frontal edge when it overtakes the MC tail (the area within the green oval). The large value of P_t at the frontal boundary of the CIR implies a high compression because of the interaction with the preceded ICME. Furthermore, the valid magnetic pressure profile F, compared to the STB magnetic pressure F′, confirms that the STB CIR witnessed a large compression in magnetic pressure at the frontal region during its travel from the STB to L1 position, in particular at the magnetic exhausted region (green shade). This raises the overall STB CIR magnetic pressure, especially the values of P1 and P2, and reduced the duration between them.

   Panels F and E2 provide details of the rise in Max magnetic pressure and the total pressure of the CIR frontal edge when it overtook the MC tail. It has changed hugely due to the interaction from the rear when the CIR is isolated (panels F′ and E′) to the leading edge after the interaction with the ICME, despite the existence of the magnetic exhausted region between the two structures.

   The similarities between magnetic field and plasma profiles emphasize that both spacecrafts traverse the same CIR pattern and that the different duration is caused by the high compression of the ICME-CIR interaction at the Earth's in situ region. The high compression characteristic of the CIR duration observed by the L1 spacecraft is shorter by about a factor of 4 and produces a fast reverse shock at the rear boundary of the CIR. The first 6 hr of the unperturbed STEREO B CIR was absenting in ACE measurements, which means that this region was out of the interaction zone.
4. Panels G and G′ show very different CIR velocity profiles, with a large contrast between the front and rear boundary in G′ (ACE proton speed is less decline, perhaps due to the expansion with the ICME), which reflects the high impact of this interaction on the CIR speed morphology more than the other solar wind parameters.
5. The values of the magnetic field and plasma at L1 Region are increased due to the high compression.

It is reasonable to expect some structural change in the CIR magnetic and particles profiles between the 6 days' separation of STEREO B and L1, even without the disruption of large ICMEs. A future study will quantify such changes through a long-term study of this CIR, which recurs over several solar rotations during 2011. During the period 4–10 September, the CIR may have been disrupted by a small number of weak CMEs accompanied by class-C flares and one CME with an M5.3 flare in addition to our main ICME event. Also, the 6 September CME was the only halo during this period. The fact that some signatures/parameters are clearly preserved while others are completely disrupted suggests a useful method for interpreting ICME-CIR interaction.

3.8. Impact of the ICME-CIR/HSS Interaction

The remote sensing observations give a possibility of CME-CME interaction, but the in situ observations support the 9–10 September 2011 event as an ICME-CIR embedded. The MC has a clear azimuthal magnetic field rotation (magnetic flux rope) and a weak southward *Bz* (*Dst* ≤ -69), which is incompatible with the ICME-ICME criteria who often have a nonsmooth magnetic rotation (Burlaga et al., 2001, 2002) and associated at Earth extended periods of strong southward *Bz* with intense geomagnetic storms (*Dst* ≤ -100 nT; Farrugia et al., 2006, 2006) or (*Dst* ≤ -200; Wang et al., 2003). In addition, the ICME- ICME can have a long duration and may drive the magnetosphere for an extended period (≥3 days; Lugaz & Farrugia, 2014), while a typical CME passes over Earth in ~24 hr (e.g., Klein & Burlaga, 1982); some events last well in excess of 30 hr (Marubashi & Lepping, 2007). The 9–10 September event (ICME- CIR) interval is about 1.5 days with a magnetic cloud duration of about 10 hr. Moreover, due to their compression and interaction, ICME-ICME events have a generally higher proton temperature than our event's MC (e.g., Lugaz et al., 2012, 2016).

The effect of the ICME-CIR/HSS interaction was clear from the magnetic strength of the rear tail of the MC. An elevation of the magnetic field magnitude formed a second magnetic pressure peak P2 (Figure 11). The first magnetic pressure peak P1 was at the front of the ICME (during the shock and the beginning of the sheath). This is also obvious at the ACE/SOHO combine total pressure profile. The role of the embedded CIR/HSS was noticeable by the very high increase of speed within the sheath at ACE between 16:39 UT, 9 September (467.7 km/s), and 17:54 UT, 9 September (596.6 km/s; see Figure 9), followed by a gradual deceleration and expansion that continues until the rear of the MC (Figure 5 panel 6), reflecting the high compression between the two interplanetary structures. This expansion and deceleration may be due to the coronal hole CH475, which caused the sheath and the MC deflect away to the west. This may also be the reason that the ICME impacted the Earth from the flank. The prominent speed increase is also obvious at Wind (Figure 10). Conversely, the SOHO speed is significantly lower than the other two. This suggests that there is some difference after 15 UT, caused either by the different spacecraft locations or by some other factor (Figures 5 and 9). The differences in velocity between spacecraft remain even after the resampling of data to matching time steps.

It was difficult to identify the stream interface (SI) because there is no significant peak of Pt profile and approximately 20% of stream interaction regions have a sharp boundary between fast and slow flows (Jian et al., 2008). We nominated three points to act as an SI based on the criteria: a decrease in proton density, a rise in proton temperature, and a flow shear and an increase in proton speed (Burlaga, 1974; Gosling et al., 1978; Jian et al., 2006b, 2008). The effect of the ICME-CIR interaction was clear insofar as none of the nominated SIs met all the major criteria in an unambiguous and obvious way, and this was probably due to the complexity of ICME-CIR interaction. One of the SIs likely occurred at 19:34 UT, DOY 253 (second vertical red dashed line). In this location, the proton density starts to decline accompanied by unclear behavior of the proton temperature. The most significant phenomena are the change in the azimuthal proton flow speed direction (*Vy*) from west to east (flow shear). Another potential apparent SI was noticed at 20:49 UT, DOY 253 (third vertical red dashed line) in the form of a reduction in the proton density accompanied by a rise in temperature and a *Vz* shear. The third nominated location was at 15:29 UT, DOY 253 (first vertical red dashed line): here a steep decrease in proton density, an increase in proton temperature, and a *Vy* flow shear. Within the CIR, there must be at least one SI (Crooker et al., 1999). We think that because of the complicated interaction, the probability of more than one SI appearing is large in this turbulent CIR region.

4. Summary and Conclusions

Over the course of the 9–10 September event, the effect of the HPS-ICME-CIR/HSS interaction was noticeable on the ICME magnetic and particles parameters morphology. Both HPS and CIR/HSS added more complexity to the ICME morphology at the in situ region, and the whole event was ICME-CIR embedded. High elevations in magnetic field magnitude and total pressure at the front of the ICME and high magnetic field magnitude rising at the and the rear formed the two significant magnetic peaks P1 and P2, respectively. The appearance of the HPS at the front of the ICME and its penetration through the ICME forward shock perhaps assisted in increasing the strength of compression regions. The general features of the magnetic field and total pressure morphology reflect the effect of the ICME interaction with the HPS at the front and the ICME interaction with

the CIR at the rear. It is also reflected in the ICME deceleration and expansion from the middle of the sheath until the MC rear boundary. These may be due to the coronal hole CH475, which made the sheath and the MC deflect away to the west and the ICME impact the Earth from the flank even though the CME was a halo. The overall interplanetary magnetic field feature was unidirectional during the event, which led us to propose an interchange reconnection scenario depending on the remote and in situ data.

A significant shift between the high-density and the magnetic field magnitude peaks at the front of the ICME. It is attributed to the HPS penetration of the ICME frontal. The ICME forward shock speed was not high, and this was because of its intra-HPS existence, which delayed the shock a little. Based on the strahl distributions and $B\phi$ morphology, there was a match between the SBC and HCS, and the HPS bordered the HCS because of the interchange reconnection. The high proton density within the HPS has attributed to the open magnetic field loop, which released the material blob in the HPS. The multiple $B\phi$ reversals during the sheath did not affect the general direction of the interplanetary magnetic field, although it lasted for several hours. The same held true for the local $B\phi$ reversals during the HPS. The multiple magnetic field reversals during the HPS interval, the high elevation of the HPS proton density, and the HPS location where it bordered rather than straddled the HCS supported the interchange reconnection. Based on the magnetic cloud and the sheath duration, the spacecraft predominantly traversed the ICME from the flank. The forward shock was strong, and the ICME speed is not enough to drive it. We attributed that the most likely source of the shock is the ICME-CIR interaction. The ICME-CIR/HSS interaction impact was distributed along the 9–10 September event in different locations with different features represented by (1) the HSS imprint on the 272-eV suprathermal electron discontinuity at the ICME frontal forward shock upstream, (2) the noticeable high-speed elevation in the middle of the sheath, (3) the magnetic cloud flux rope *B*z rotation distortion, (4) ICME unidirectional suprathermal electrons distribution due to the interchange reconnection, and (5) difficulty determining the stream interaction (SI). Three potential SIs were nominated.

This event is very unusual. There are considerable differences in the timing of proton density and temperature features between spacecraft. The SOHO proton speed before ~18 UT, 9 September, is significantly lower than the other L1 spacecraft, and the Wind forward shock density is much larger than at SOHO, which is likely to be due to the difference in the spacecraft locations or the fluctuations in the interplanetary magnetic field.

On 4 September 2011, STB recorded a CIR passage. The HSS resource was the same coronal hole. A significant matching was noted in the CIR's physical parameter morphologies of both 4 and 10 September, and this means that both STB and ACE traverse the same CIR spiral pattern with different durations because of the L1 ICME-CIR interaction. The compression made the ACE CIR duration shorter by about a factor of 4, and some of the CIR physical parameters value has changed. The survival of a magnetic exhausted region at the front of the CIR before and with the interaction suggests that care must be taken in the interpretation of many other similar cases. Accurate interpretation of many complex in situ interaction events is difficult without a comparison of events in the absence of interaction.

The main finding of the study is that the interaction has its impact on all the three interplanetary structures with varying proportions. The major features are the following: the unusual density of the HPS, the ability to drive a strong forward shock, the unidirectional heat flux along the event, the *B*z distortion of the MC, the reverse shock, and the high compression of factor 4 of the CIR.

Acknowledgments
We are grateful to Skoug, Ruth M., and Lan K. Jian for their helpful comments. The solar wind magnetic field and plasma data are courtesy of the ACE MAG and SWEPAM, the Wind MFI and SWE, and the STEREO IMPACT and PLASTIC teams.

References

Andrews, G. B., Zurbuchen, T. H., Mauk, B. H., Malcom, H., Fisk, L. A., Gloeckler, G., et al. (2007). The Energetic Particle and Plasma Spectrometer Instrument on the MESSENGER Spacecraft. *Space Science Reviews*, *131*(1-4), 523–556. https://doi.org/10.1007/s11214-007-9272-5

Blanco, J., Rodríguez-Pacheco, J., Hidalgo, M., & Sequeiros, J. (2006). Analysis of the heliospheric current sheet fine structure: Single or multiple current sheets. *Journal of Atmospheric and Solar-Terrestrial Physics*, *68*(18), 2173–2181. https://doi.org/10.1016/j.jastp.2006.08.007

Bothmer, V., & Rust, D. (1997). The field configuration of magnetic clouds and the solar cycle. In N. Crooker, J. A. Joselyn, & J. Feynman (Eds.), *Coronal mass ejections* (pp. 139–146). Washington, DC: American Geophysical Union. https://doi.org/10.1029/GM099p0139

Brueckner, G., Howard, R., Koomen, M., Korendyke, C., Michels, D., Moses, J., et al. (1995). The Large Angle Spectroscopic Coronagraph (LASCO). *Solar Physics*, *162*(1-2), 357–402. https://doi.org/10.1007/BF00733434

Burlaga, L. (1974). Interplanetary stream interfaces. *Journal of Geophysical Research*, *79*, 3717–3725. https://doi.org/10.1029/JA079i025p03717

Burlaga, L., Behannon, K., & Klein, L. (1987). Compound streams, magnetic clouds, and major geomagnetic storms. *Journal of Geophysical Research*, *92*, 5725–5734. https://doi.org/10.1029/JA092iA06p05725

Burlaga, L., Fitzenreiter, R., Lepping, R., Ogilvie, K., Szabo, A., Lazarus, A., et al. (1998). A magnetic cloud containing prominence material: January 1997. *Journal of Geophysical Research*, *103*, 277–285. https://doi.org/10.1029/97JA02768

Burlaga, L., Plunkett, S., & St Cyr, O. (2002). Successive CMEs and complex ejecta. *Journal of Geophysical Research*, *107*(A10), 1266. https://doi.org/10.1029/2001JA000255

Burlaga, L., Sittler, E., Mariani, F., & Schwenn, R. (1981). Magnetic loop behind an interplanetary shock: Voyager, Helios, and IMP 8 observations. *Journal of Geophysical Research*, *86*, 6673–6684. https://doi.org/10.1029/JA086iA08p06673

Burlaga, L., Skoug, R., Smith, C., Webb, D., Zurbuchen, T., & Reinard, A. (2001). Fast ejecta during the ascending phase of solar cycle 23: ACE observations, 1998–1999. *Journal of Geophysical Research*, *106*, 20,957–20,977. https://doi.org/10.1029/2000JA000214

Crooker, N., Burton, M., Siscoe, G., Kahler, S., Gosling, J., & Smith, E. (1996). Solar wind streamer belt structure. *Journal of Geophysical Research*, *101*, 24,331–24,341. https://doi.org/10.1029/96JA02412

Crooker, N., Gosling, J., Bothmer, V., Forsyth, R., Gazis, P., Hewish, A., et al. (1999). CIR morphology, turbulence, discontinuities, and energetic particles. *Space Science Reviews*, *89*(1/2), 179–220. https://doi.org/10.1023/A:1005253526438

Crooker, N., Gosling, J., & Kahler, S. (2002). Reducing heliospheric magnetic flux from coronal mass ejections without disconnection. *Journal of Geophysical Research*, *107*(A2), 1028. https://doi.org/10.1029/2001JA000236

Crooker, N., Huang, C. L., Lamassa, S., Larson, D., Kahler, S., & Spence, H. E. (2004). Heliospheric plasma sheets. *Journal of Geophysical Research*, *109*, A03107. https://doi.org/10.1029/2003JA010170

Crooker, N., Kahler, S., Larson, D., & Lin, R. (2004). Large-scale magnetic field inversions at sector boundaries. *Journal of Geophysical Research*, *109*, A03108. https://doi.org/10.1029/2003JA010278

Domingo, V., Fleck, B., & Poland, A. I. (1995). The SOHO mission: an overview. *Solar Physics*, *162*(1-2), 1–37. https://doi.org/10.1007/BF00733425

Farrugia, C., Berdichevsky, D., Möstl, C., Galvin, A., Leitner, M., Popecki, M., et al. (2011). Multiple, distant (40) in situ observations of a magnetic cloud and a corotating interaction region complex. *Journal of Atmospheric and Solar-Terrestrial Physics*, *73*(10), 1254–1269. https://doi.org/10.1016/j.jastp.2010.09.011

Farrugia, C., Jordanova, V., Thomsen, M., Lu, G., Cowley, S., & Ogilvie, K. (2006). A two-ejecta event associated with a two-step geomagnetic storm. *Journal of Geophysical Research*, *111*, A11104. https://doi.org/10.1029/2006JA011893

Farrugia, C., Matsui, H., Kucharek, H., Jordanova, V., Torbert, R., Ogilvie, K., et al. (2006). Survey of intense Sun–Earth connection events (1995–2003). *Advances in Space Research*, *38*(3), 498–502. https://doi.org/10.1016/j.asr.2005.05.051

Fisk, L. (2005). The open magnetic flux of the Sun: I. Transport by reconnections with coronal loops. *The Astrophysical Journal*, *626*(1), 563–573. https://doi.org/10.1086/429957

Gopalswamy, N. (2006). Properties of interplanetary coronal mass ejections. *Space Science Reviews*, *124*, 145–168.

Gopalswamy, N., & Kundu, M. (1992). Estimation of the mass of a coronal mass ejection from radio observations. *The Astrophysical Journal*, *390*, L37–L39. https://doi.org/10.1086/186366

Gopalswamy, N., Mäkelä, P., Xie, H., Akiyama, S., & Yashiro, S. (2009). CME interactions with coronal holes and their interplanetary consequences. *Journal of Geophysical Research*, *114*, A00A22. https://doi.org/10.1029/2008JA013686

Gosling, J., Asbridge, J., Bame, S., & Feldman, W. (1978). Solar wind stream interfaces. *Journal of Geophysical Research*, *83*, 1401–1412. https://doi.org/10.1029/JA083iA04p01401

Gosling, J., Bame, S., Mccomas, D., Phillips, J., Pizzo, V., Goldstein, B., & Neugebauer, M. (1993). Latitudinal variation of solar wind corotating stream interaction regions: Ulysses. *Geophysical Research Letters*, *20*, 2789–2792. https://doi.org/10.1029/93GL03116

Gosling, J., Birn, J., & Hesse, M. (1995). Three-dimensional magnetic reconnection and the magnetic topology of coronal mass ejection events. *Geophysical Research Letters*, *22*, 869–872. https://doi.org/10.1029/95GL00270

Gosling, J., Eriksson, S., & Schwenn, R. (2006). Petschek-type magnetic reconnection exhausts in the solar wind well inside 1 AU: Helios. *Journal of Geophysical Research*, *111*, A10102. https://doi.org/10.1029/2006JA011863

Gosling, J., Hundhausen, A., & Bame, S. (1976). Solar-wind stream evolution at large heliocentric distances-experimental demonstration and test of a model. *Journal of Geophysical Research*, *81*, 2111–2122. https://doi.org/10.1029/JA081i013p02111

Gosling, J., & Pizzo, V. (1999). Formation and evolution of corotating interaction regions and their three dimensional structure. In *Corotating interaction regions* (pp. 21–52). Springer. https://doi.org/10.1007/978-94-017-1179-1_3

Gosling, J., Skoug, R., & Feldman, W. (2001). Solar wind electron halo depletions at 90 pitch angle. *Geophysical Research Letters*, *28*, 4155–4158. https://doi.org/10.1029/2001GL013758

Gosling, J., Skoug, R., Mccomas, D., & Smith, C. (2005). Direct evidence for magnetic reconnection in the solar wind near 1 AU. *Journal of Geophysical Research*, *110*, A01107. https://doi.org/10.1029/2004JA010809

Gosling, J. T., Borrini, G., Asbridge, J. R., Bame, S. J., Feldman, W. C., & Hansen, R. T. (1981). Coronal streamers in the solar wind at 1 AU. *Journal of Geophysical Research*, *86*, 5438–5448. https://doi.org/10.1029/JA086iA07p05438

Guerrero, A., Cid, C., Cerrato, Y., Saiz, E., Palacios, J., & Seaton, D. (2012). Geoeffectiveness of two CMEs interacting with the same CH. *Geophysical Research Abstracts, Vol. 14, EGU2012-9720,* EGU General Assembly.

Harra, L. K., Crooker, N. U., Mandrini, C. H., Van Driel-Gesztelyi, L., Dasso, S., Wang, J., et al. (2007). How does large flaring activity from the same active region produce oppositely directed magnetic clouds? *Solar Physics*, *244*, 95–114.

Howard, R., Moses, J., Socker, D., Dere, K., Cook, J., & Consortium, S. (2002). Sun Earth Connection Coronal and Heliospheric Investigation (SECCHI). *Advances in Space Research*, *29*, 2017–2026.

Hu, Y., & Jia, X. (2001). Interplanetary shock interaction with the heliospheric current sheet and its associated structures. *Journal of Geophysical Research*, *106*, 29,299–29,304. https://doi.org/10.1029/2001JA000112

Hudson, H., Acton, L., & Freeland, S. (1996). A long-duration solar flare with mass ejection and global consequences. *The Astrophysical Journal*, *470*, 629. https://doi.org/10.1086/177894

Hundhausen, A., & Gosling, J. (1976). Solar wind structure at large heliocentric distances: An interpretation of Pioneer 10 observations. *Journal of Geophysical Research*, *81*, 1436–1440. https://doi.org/10.1029/JA081i007p01436

Ipavich, F. M., Galvin, A. B., Lasley, S. E., Paquette, J. A., Hefti, S., Reiche, K. U., et al. (1998). Solar wind measurements with SOHO: The CELIAS/MTOF proton monitor. *Journal of Geophysical Research*, *103*, 17,205–17,213. https://doi.org/10.1029/97JA02770

Jian, L., Russell, C., Luhmann, J., & Skoug, R. (2006a). Properties of interplanetary coronal mass ejections at one AU during 1995–2004. *Solar Physics*, *239*(1-2), 393–436. https://doi.org/10.1007/s11207-006-0133-2

Jian, L., Russell, C., Luhmann, J., & Skoug, R. (2006b). Properties of stream interactions at one AU during 1995–2004. *Solar Physics*, *239*(1-2), 337–392. https://doi.org/10.1007/s11207-006-0132-3

Jian, L., Russell, C., Luhmann, J., & Skoug, R. (2008). Evolution of solar wind structures from 0.72 to 1AU. *Advances in Space Research*, *41*(2), 259–266. https://doi.org/10.1016/j.asr.2007.03.023

Jian, L., Russell, C., Luhmann, J., Skoug, R., & Steinberg, J. (2008). Stream interactions and interplanetary coronal mass ejections at 0.72 AU. *Solar Physics*, *249*(1), 85–101. https://doi.org/10.1007/s11207-008-9161-4

Jiang, C., Feng, X., Wu, S., & Hu, Q. (2013). Magnetohydrodynamic simulation of a sigmoid eruption of active region 11283. *The Astrophysical Journal Letters*, *771*(2), L30. https://doi.org/10.1088/2041-8205/771/2/L30

Kahler, S., Crocker, N., & Gosling, J. (1996). The topology of intrasector reversals of the interplanetary magnetic field. *Journal of Geophysical Research*, *101*, 24,373–24,382. https://doi.org/10.1029/96JA02232

Kahler, S., & Lin, R. (1994). The determination of interplanetary magnetic field polarities around sector boundaries using E> 2 keV electrons. *Geophysical Research Letters*, *21*, 1575–1578. https://doi.org/10.1029/94GL01362

Kahler, S., & Lin, R. (1995). An examination of directional discontinuities and magnetic polarity changes around interplanetary sector boundaries usingE> 2 keV electrons. *Solar Physics*, *161*(1), 183–195. https://doi.org/10.1007/BF00732092

Kaiser, M. (2005). The STEREO mission: An overview. *Advances in Space Research*, *36*(8), 1483–1488. https://doi.org/10.1016/j.asr.2004.12.066

Khabarova, O., & Zastenker, G. (2011). Sharp changes of solar wind ion flux and density within and outside current sheets. *Solar Physics*, *270*(1), 311–329. https://doi.org/10.1007/s11207-011-9719-4

Klein, L. W., & Burlaga, L. F. (1982). Interplanetary magnetic clouds At 1 AU. *Journal of Geophysical Research*, *87*, 613–624. https://doi.org/10.1029/JA087iA02p00613

Krieger, A., Timothy, A., & Roelof, E. (1973). A coronal hole and its identification as the source of a high velocity solar wind stream. *Solar Physics*, *29*(2), 505–525. https://doi.org/10.1007/BF00150828

Lemen, J. R., Akin, D. J., Boerner, P. F., Chou, C., Drake, J. F., Duncan, D. W., et al. (2011). The atmospheric imaging assembly (AIA) on the solar dynamics observatory (SDO). In *The solar dynamics observatory* (pp. 17–40). Springer. https://doi.org/10.1007/978-1-4614-3673-7_3

Lepping, R., Acũna, M., Burlaga, L., Farrell, W., Slavin, J., Schatten, K., et al. (1995). The WIND magnetic field investigation. *Space Science Reviews*, *71*(1-4), 207–229. https://doi.org/10.1007/BF00751330

Lepping, R., Burlaga, L., Szabo, A., Ogilvie, K., Mish, W., Vassiliadis, D., et al. (1997). The Wind magnetic cloud and events of October 18–20, 1995: Interplanetary properties and as triggers for geomagnetic activity. *Journal of Geophysical Research*, *102*, 14,049–14,063. https://doi.org/10.1029/97JA00272

Liu, Y. M., Huang, J., Wang, C., Klecker, B., Galvin, A., Simunac, K., et al. (2014). A statistical analysis of heliospheric plasma sheets, heliospheric current sheets, and sector boundaries observed in situ by STEREO. *Journal of Geophysical Research*, *119*, 8721–8732. https://doi.org/10.1002/2014JA019956

Lugaz, N., & Farrugia, C. (2014). A new class of complex ejecta resulting from the interaction of two CMEs and its expected geoeffectiveness. *Geophysical Research Letters*, *41*, 769–776. https://doi.org/10.1002/2013GL058789

Lugaz, N., Farrugia, C., Davies, J., Möstl, C., Davis, C., Roussev, I., & Temmer, M. (2012). The deflection of the two interacting coronal mass ejections of 2010 May 23-24 as revealed by combined in situ measurements and heliospheric imaging. *The Astrophysical Journal*, *759*(1), 68. https://doi.org/10.1088/0004-637X/759/1/68

Lugaz, N., Temmer, M., Wang, Y., & Farrugia, C. J. (2016). The interaction of successive coronal mass ejections: A review. *arXiv preprint arXiv:1612.02398*

Luhmann, J., Curtis, D., Schroeder, P., Mccauley, J., Lin, R., Larson, D., et al. (2008). STEREO IMPACT investigation goals, measurements, and data products overview. *Space Science Reviews*, *136*(1-4), 117–184. https://doi.org/10.1007/s11214-007-9170-x

Marubashi, K., & Lepping, R. (2007). Long-duration magnetic clouds: a comparison of analyses using torus-and cylinder-shaped flux rope models. *Annales Geophysicae*, *25*(11), 2453–2477. https://doi.org/10.5194/angeo-25-2453-2007

Mccomas, D., Bame, S., Barker, P., Feldman, W., Phillips, J., Riley, P., & Griffee, J. (1998). Solar Wind Electron Proton Alpha Monitor (SWEPAM) for the Advanced Composition Explorer. In *The Advanced Composition Explorer Mission* (pp. 563–612). Springer. https://doi.org/10.1007/978-94-011-4762-0_20

Mccomas, D. J., Gosling, J. T., Phillips, J. L., Bame, S. J., Luhmann, J. G., & Smith, E. J. (1989). Electron heat flux dropouts in the solar wind: Evidence for interplanetary magnetic field reconnection? *Journal of Geophysical Research*, *94*, 6907–6916. https://doi.org/10.1029/JA094iA06p06907

Mitsakou, E., & Moussas, X. (2014). Statistical study of ICMES and their sheaths during solar cycle 23 (1996–2008). *Solar Physics*, *289*(8), 3137–3157. https://doi.org/10.1007/s11207-014-0505-y

Morgan, H. (2011). The rotation of the white light solar corona at height 4 $R_\odot$ from 1996 to 2010: A tomographical study of large angle and spectrometric coronagraph C2 observations. *The Astrophysical Journal*, *738*(2), 189. https://doi.org/10.1088/0004-637X/738/2/189

Morgan, H., & Druckmüller, M. (2014). Multi-scale Gaussian normalization for solar image processing. In *Coronal magnetometry* (pp. 2945–2955). Springer. https://doi.org/10.1007/978-1-4939-2038-920

Morgan, H., & Habbal, S. R. (2010). Observational aspects of the three-dimensional coronal structure over a solar activity cycle. *The Astrophysical Journal*, *710*(1), 1–15. https://doi.org/10.1088/0004-637X/710/1/1

Morgan, H., Habbal, S. R., & Woo, R. (2006). The depiction of coronal structure in white-light images. *Solar Physics*, *236*(2), 263–272. https://doi.org/10.1007/s11207-006-0113-6

Morgan, H., Jeska, L., & Leonard, D. (2013). The expansion of active regions into the extended solar corona. *The Astrophysical Journal Supplement Series*, *206*(2), 19. https://doi.org/10.1088/0067-0049/206/2/19

Mulligan, T., Russell, C., & Luhmann, J. (1998). Solar cycle evolution of the structure of magnetic clouds in the inner heliosphere. *Geophysical Research Letters*, *25*, 2959–2962. https://doi.org/10.1029/98GL01302

Neugebauer, M., Liewer, P., Goldstein, B., Zhou, X., & Steinberg, J. (2004). Solar wind stream interaction regions without sector boundaries. *Journal of Geophysical Research*, *109*, A10102. https://doi.org/10.1029/2004JA010456

Ogilvie, K., Chornay, D., Fritzenreiter, R., Hunsaker, F., Keller, J., Lobell, J., et al. (1995). SWE, a comprehensive plasma instrument for the Wind spacecraft. *Space Science Reviews*, *71*(1-4), 55–77. https://doi.org/10.1007/BF00751326

Parker, E. N. (1963). *Interplanetary dynamical processes* (p. 1). New York: Interscience Publishers.

Pesnell, W. D. (2015). Solar dynamics observatory (SDO). In *Handbook of Cosmic Hazards and Planetary Defense* (pp.179–196).

Pizzo, V. (1978). A three-dimensional model of corotating streams in the solar wind: 1. Theoretical foundations. *Journal of Geophysical Research*, *83*, 5563–5572. https://doi.org/10.1029/JA083iA12p05563

Richardson, I., & Cane, H. (1995). Regions of abnormally low proton temperature in the solar wind (1965–1991) and their association with ejecta. *Journal of Geophysical Research*, *100*, 23,397–23,412. https://doi.org/10.1029/95JA02684

Richardson, I., & Cane, H. (2010). Near-Earth interplanetary coronal mass ejections during solar cycle 23 (1996–2009): Catalog and summary of properties. *Solar Physics*, *264*(1), 189–237. https://doi.org/10.1007/s11207-010-9568-6

Rouillard, A., Savani, N., Davies, J., Lavraud, B., Forsyth, R., Morley, S., et al. (2009). A multispacecraft analysis of a small-scale transient entrained by solar wind streams. *Solar Physics*, *256*(1-2), 307–326. https://doi.org/10.1007/s11207-009-9329-6

Rouillard, A. P., Lavraud, B., Davies, J. A., Savani, N. P., Burlaga, L. F., Forsyth, R. J., et al. (2010). Intermittent release of transients in the slow solar wind: 2. In situ evidence. *Journal of Geophysical Research*, *115*, A04104. https://doi.org/10.1029/2009JA014472

Russell, C., Shinde, A., & Jian, L. (2005). A new parameter to define interplanetary coronal mass ejections. *Advances in Space Research*, *35*(12), 2178–2184. https://doi.org/10.1016/j.asr.2005.04.024

Sauvaud, J.-A., Larson, d., Aoustin, C., Curtis, D., Médale, J.-L., Fedorov, A., et al. (2008). The IMPACT solar wind electron analyzer (SWEA). In *The STEREO Mission* (pp. 227–239). Springer. https://doi.org/10.1007/978-0-387-09649-0_9

Scherrer, P. H., Schou, J., Bush, R., Kosovichev, A., Wrt, R., Hoeksema, J., et al. (2011). The helioseismic and magnetic imager (HMI) investigation for the solar dynamics observatory (SDO) (pp. 207–227). In *The Solar Dynamics Observatory*. Springer.

Schwenn, R. (1990). Large-scale structure of the interplanetary medium. In *Physics of the inner Heliosphere I* (pp. 99–181). Springer.

Shodhan, S., Crooker, N., Kahler, S., Fitzenreiter, R., Larson, D., Lepping, R., et al. (2000). Counterstreaming electrons in magnetic clouds. *Journal of Geophysical Research*, *105*, 27,261–27,268. https://doi.org/10.1029/2000JA000060

Simunac, K., Galvin, A., Farrugia, C., Kistler, L., Kucharek, H., Lavraud, B., et al. (2012). The heliospheric plasma sheet observed in situ by three spacecraft over four solar rotations. *Solar Physics*, *281*, 423–447.

Siscoe, G., & Intriligator, D. (1993). Three views of two giant streams: Aligned observations at 1 AU, 4.6 AU, and 5.9 AU. *Geophysical Research Letters*, *20*, 2267–2270. https://doi.org/10.1029/93GL02488

Skoug, R., Gosling, J., Mccomas, D., Smith, C., & Hu, Q. (2006). Suprathermal electron 90 pitch angle depletions at reverse shocks in the solar wind. *Journal of Geophysical Research*, *111*, A01101. https://doi.org/10.1029/2005JA011316

Smith, C. W., L'heureux, J., Ness, N. F., Acuña, M. H., Burlaga, L. F., & Scheifele, J. (1998). The ACE magnetic fields experiment. In *The Advanced Composition Explorer Mission* (pp. 613–632). Springer. https://doi.org/10.1007/978-94-011-4762-0_21

Smith, E. J., & Wolfe, J. H. (1976). Observations of interaction regions and corotating shocks between one and five AU: Pioneers 10 and 11. *Geophysical Research Letters*, *3*, 137–140. https://doi.org/10.1029/GL003i003p00137

Smith, Z., Odstrcil, D., & Dryer, M. (1998). A 2.5-dimensional MHD parametric study of interplanetary shock interactions with the heliospheric current sheet/heliospheric plasma sheet. *Journal of Geophysical Research*, *103*, 20,581–20,589. https://doi.org/10.1029/98JA01994

Song, H., Chen, Y., Liu, K., Feng, S., & Xia, L. (2009). Quasi-periodic releases of streamer blobs and velocity variability of the slow solar wind near the Sun. *Solar Physics*, *258*(1), 129–140. https://doi.org/10.1007/s11207-009-9411-0

Steinberg, J., Gosling, J., Skoug, R., & Wiens, R. (2005). Suprathermal electrons in high-speed streams from coronal holes: Counterstreaming on open field lines at 1 AU. *Journal of Geophysical Research*, *110*, A06103. https://doi.org/10.1029/2005JA011027

Stone, E., Frandsen, A., Mewaldt, R., Christian, E., Margolies, D., Ormes, J., & Snow, F. (1998). The advanced composition explorer. In *The Advanced Composition Explorer Mission* (pp. 1–22). Springer. https://doi.org/10.1007/978-94-011-4762-0_1

Suess, S., Ko, Y. K., Von Steiger, R., & Moore, R. (2009). Quiescent current sheets in the solar wind and origins of slow wind. *Journal of Geophysical Research*, *114*, A04103. https://doi.org/10.1029/2008JA013704

Svalgaard, L., & Wilcox, J. M. (1975). Long term evolution of solar sector structure. *Solar Physics*, *41*(2), 461–475. https://doi.org/10.1007/BF00154083

Wang, Y.-M., & Sheeley Jr, N. (2003). On the topological evolution of the coronal magnetic field during the solar cycle. *The Astrophysical Journal*, *599*(2), 1404–1417. https://doi.org/10.1086/379348

Wang, Y. M., Sheeley, N., Socker, D., Howard, R., & Rich, N. (2000). The dynamical nature of coronal streamers. *Journal of Geophysical Research*, *105*, 25,133–25,142. https://doi.org/10.1029/2000JA000149

Wang, Y. M., Ye, P. Z., & Wang, S. (2003). Multiple magnetic clouds: Several examples during March–April 2001. *Journal of Geophysical Research*, *108*(A10), 1370. https://doi.org/10.1029/2003JA009850

Watanabe, T. (1989). Solar wind latitude/longitude variations derived from interplanetary scintillations. *Advances in Space Research*, *9*, 99–110.

Wei, F., Liu, R., Fan, Q., & Feng, X. (2003). Identification of the magnetic cloud boundary layers. *Journal of Geophysical Research*, *108*(A6), 1263. https://doi.org/10.1029/2002JA009511

Weimer, D., Ober, D., Maynard, N., Burke, W., Collier, M., Mccomas, D., et al. (2002). Variable time delays in the propagation of the interplanetary magnetic field. *Journal of Geophysical Research*, *107*(A8), 1210. https://doi.org/10.1029/2001JA009102

Weimer, D., Ober, D., Maynard, N., Collier, M., Mccomas, D., Ness, N., et al. (2003). Predicting interplanetary magnetic field (IMF) propagation delay times using the minimum variance technique. *Journal of Geophysical Research*, *108*(A1), 1026. https://doi.org/10.1029/2002JA009405

Weimer, D. R., & King, J. H. (2008). Improved calculations of interplanetary magnetic field phase front angles and propagation time delays. *Journal of Geophysical Research*, *113*, A01105. https://doi.org/10.1029/2007JA012452

Wilcox, J. M., & Ness, N. F. (1965). Quasi-stationary corotating structure in the interplanetary medium. *Journal of Geophysical Research*, *70*, 5793–5805. https://doi.org/10.1029/JZ070i023p05793

Winslow, R. M., Lugaz, N., Schwadron, N. A., Farrugia, C. J., Yu, W., Raines, J. M., et al. (2016). Longitudinal conjunction between MESSENGER and STEREO A: development of ICME complexity through stream interactions. *Journal of Geophysical Research: Space Physics*, *121*, 6092–6106. https://doi.org/10.1002/2015JA022307

Winterhalter, D., Smith, E., Burton, M., Murphy, N., & Mccomas, D. (1994). The heliospheric plasma sheet. *Journal of Geophysical Research*, *99*, 6667–6680. https://doi.org/10.1029/93JA03481

Wu, C.-C., Liou, K., Vourlidas, A., Plunkett, S., Dryer, M., Wu, S. T., et al. (2016). Numerical simulation of multiple CME-driven shocks in the month of 2011 September. *Journal of Geophysical Research: Space Physics*, *121*, 1839–1856. https://doi.org/10.1002/2015JA021843

Xu, X., Wei, F., & Feng, X. (2011). Observations of reconnection exhausts associated with large-scale current sheets within a complex ICME at 1 AU. *Journal of Geophysical Research*, *116*, A05105. https://doi.org/10.1029/2010JA016159

Zhang, J., Hess, P., & Poomvises, W. (2013). A comparative study of coronal mass ejections with and without magnetic cloud structure near the Earth: Are all interplanetary CMEs flux ropes? *Solar Physics*, *284*(1), 89–104. https://doi.org/10.1007/s11207-013-0242-7

Zurbuchen, T. H., & Richardson, i. G. (2006). In-situ solar wind and magnetic field signatures of interplanetary coronal mass ejections. *Space Science Reviews*, *123*(1-3), 31–43. https://doi.org/10.1007/s11214-006-9010-4